Assessing the effect of degeneration on the human lumbar inter-lamellar matrix

BY

USHMITA REEBYE

Masters Thesis

Principal Supervisor: Associate Professor John J. Costi

Associate Supervisor: Mr. Michael Russo

Submitted to the College of Engineering and Science for the degree of Master of Engineering (Biomedical) at Flinders University

July 18, 2022

Table of Contents

Abstract

Disc degeneration of the lumbar spine is considered as one of the underlying factors of low back pain (LBP). LBP caused by disc degeneration is known to affect an increasing number of people over 60 years each year. LBP is a billion-dollar problem that has become a huge socioeconomic burden in many countries, making it a global health threat. To date, there is little understanding of the underlying mechanism of disc degeneration from a micro-mechanical point of view. Therefore, the aim of this study was to investigate the effect of degeneration on the micromechanical properties of human inter-lamellar matrix (ILM). The ILM is the boundary between lamellae and is thought to be the weakest structure of the disc. As a result, when the disc is under compressive loads, the region at highest risk of failure is the ILM. The purpose of this research is to determine the viscoelastic and failure properties of the ILM. A validated testing method was adapted using a micromechanical testing machine to measure the viscoelastic and failure properties of the ILM in healthy and degenerated discs. The outer anterior and posterolateral region of each disc was separated, sliced and loaded under three different strain rates of 0.1%/s (slow), 1%/s (medium) and 10%/s (fast). Uniaxial testing in tension (radial) and shear (circumferential) directions was preformed, followed by failure tests. Outcome measures of modulus and energy absorption (hysteresis loss coefficient) were obtained from the dynamic tests, followed by the failure test parameters of failure stress and toughness. The anisotropic structure of the ILM was confirmed since different behaviors of tensile and shear modulus were observed for both healthy and degenerated discs. In addition, when disc regions were compared, both tensile and shear modulus were lower in the posterolateral region indicating that this region was more susceptible to failure. When tested to failure, the ILM demonstrated a significantly lower failure shear stress compared to tensile stress, thus supporting the understanding that discs are more vulnerable under shear stresses. The results of this study enhanced our knowledge about the mechanics of the ILM in healthy and degenerated discs and can be used for a better understanding of the initiation and progression of delamination that result in degeneration.

Declaration

I certify that this thesis:

1. does not incorporate without acknowledgment any material previously submitted for a degree or diploma in any university
2. and the research within will not be submitted for any other future degree or diploma without the permission of Flinders University; and
3. to the best of my knowledge and belief, does not contain any material previously published or written by another person except where due reference is made in the text.

Signature of student.....

Print name of student.....Ushmita Devi Reebye

Date.....18 July 2022.....

I certify that I have read this thesis. In my opinion it is/is not (please circle) fully adequate, in scope and in quality, as a thesis for the degree of <Degree Name>. Furthermore, I confirm that I have provided feedback on this thesis and the student has implemented it minimally/partially/fully (please circle).

Signature of Principal Supervisor.....

Print name of Principal Supervisor.....

Date.....

Acknowledgements

I would like to express my special thanks of gratitude to my primary supervisor Associate Professor John J. Costi for his guidance and continuous support during my research. I would also like to thank my secondary supervisor, Mr. Michael Russo for his invaluable patience and immerse knowledge. I could not ask for a better team- I believe I learned from the best.

To all the amazing friends I made throughout this journey, especially Ali Kaissi, Atefa Rezwani, Tirad Alsharari, thank you for your continuous moral support. It has been a pleasure to work with you all.

Finally, I would like to thank my parents for their love and support throughout my life. My sisters deserve my wholehearted thanks as well. Their belief in me has kept my spirits and motivation high during this process. To my partner, thank you for your understanding and encouragement in my many, many moments of crisis.

List of Figures

Introduction

Intervertebral discs undergo gradual disc degeneration which alters its geometric morphology and biomechanical behavior (Adams and Roughley, 2006). This degenerative effect eventually impairs the disc's capacity to transfer and distribute loads, which can lead to lower back pain (LBP). It is known that LBP affects the lumbar regions the most. Ageing, excessive mechanical loads, and accidental damage are just a few of the mechanisms that can lead to or accelerate disc degeneration (Stokes and Iatridis, 2004, Iatridis et al., 1997, Wilke et al., 2006). LBP caused by disc degeneration is known to affect a growing number of people aged 60 years or above each year (Waris et al., 2007, Walker, 2000). Being a billion-dollar problem, LBP is considered as a global health threat as it has developed into a huge socioeconomic burden in many nations (Deyo et al., 2005). Therefore, a better understanding of the disc's mechanical changes, and its constituents' parts during degeneration can provide new insight on how this vital tissue behaves.

The intervertebral disc (disc) is a complex, robust structure comprising of vertebral endplates (VEP), a fibrocartilaginous annulus fibrosus (AF), and a highly hydrated nucleus pulposus (NP) (Figure 1). The AF, which is a collagenous ringed structure encloses the NP inside the disc's boundaries. When the disc experiences daily loads, the hydrated nucleus works as a shock absorber and distribute these loads out to the AF. The pressure in the NP increases and causes the disc to deform outwards to impart stability in multiaxial directions of loading. This deformation results in both shear and tensile strain of the layers of the AF as well as the boundary between lamellae (i.e., the inter-lamellar matrix (ILM)). In a degenerated disc, the shear strain can lead to separation of lamellae (delamination). Delamination is a known failure mechanism of composite, laminate structures, suggesting that the region at highest risk of failure initiation is at the ILM (Tavakoli et al., 2016). This failure initiation could potentially lead to or accelerate disc degeneration.

Figure removed due to copyright restriction.

Figure 1: Disc anatomy: The disc is comprised of vertebral endplates, a fibrocartilaginous annulus fibrosus, and a highly hydrated nucleus pulposus. Lamellae are found in the cross-sectional region of the AF.

AF delamination, being a factor of or independent of disc degeneration, is strongly associated to the ILM's structural integrity (Osti et al., 1992, Ciapetti et al., 2012). Determining the loading conditions that put the AF at risk of delamination and consequent disc disruption requires an understanding of the ILM structure. The connectivity and structure of the ILM have been investigated using a variety of destructive and non-destructive methods (Bruehlmann et al., 2004, Cassidy et al., 1989, Marchand and Ahmed, 1990, Yu et al., 2002). These studies were conducted on animal tissues, however, the human ILM mechanical role in the AF has not been extensively studied.

Therefore, the aim of this study was to ***investigate the effect of degeneration on the micromechanical properties of human ILM.*** A validated testing method was adapted using a micromechanical testing machine (BioTester, CellScale, Waterloo, ON, Canada) to measure the viscoelastic and failure properties of the ILM in ovine discs (Tavakoli et al., 2018). The discs were loaded under three different strain rates in tension (radial) and shear (circumferential) directions to determine viscoelastic properties, followed by failure tests. The following hypothesises were proposed: The ILM will exhibit viscoelastic behavior with increasing modulus and decreasing toughness and failure stress with degeneration. This new knowledge would help to better understand the mechanics behind degeneration, thus providing important data for tissue engineering and repair strategies.

Literature Review

Disc structure

Previous literature found that the region at highest risk of failure initiation is at the boundary between lamellae, which is the ILM (Figure 2) (Tavakoli et al., 2016). When the disc is under compression, the matrix experiences shear (circumferential) strain when the layers attempt to slide with respect to one another and tensile (radial) strain when these layers resist separation of the lamellae. The research conducted by Tavakoli showed that the ILM was at the highest risk of failure under those loading conditions. In the case of AF, delamination is usually seen in cases of degeneration (Adams and Roughley, 2006, Fazzalari et al., 2001). Understanding structure-function interactions, that is, understanding the relationship between the structure of the disc and its corresponding mechanical properties, at the tissue level is crucial for the development of engineered constructs as well as for understanding how normal tissue functions and how the degenerative process affects it. The effect of degeneration was investigated and proved that degeneration increases circumferential and radial failure strains, particularly in the posterolateral AF compared to the anterior AF (Tsantrizos et al., 2005, Costi et al., 2007, Amin et al., 2019).

Figure removed due to copyright restriction.

Figure 2: Structure of the disc showing regions (Anterior and Posterolateral) and loading direction (Radial and Circumferential) used in this research (Adams, 2006).

Effect of degeneration

There is little understanding of the underlying mechanism of disc degeneration from a micro-mechanical point of view. Previous research examined the impact of degeneration on the internal mechanics of human disc by using in vivo (Nachemson, 1965) and in vitro (McNally and Adams, 1992, Adams and Roughley, 2006, Skrzypiec et al., 2007) pressure measurements with thin transducers inserted into the IVD. According to these studies, degeneration affected the NP's stability to distribute load to the AF due to the NP having less water content. The assessment of disc degeneration is mostly based on the water content of the NP (Pfirrmann, Metzdorf et al. 2001). With severe degeneration, there was no clear visual distinction between the NP and AF. To differentiate between different grades of degeneration Pfirrmann devised a grading system for disc degeneration known as the 5-level Pfirrmann grading system (Table 1). Grades 1-2 are considered as healthy discs where the NP and AF can be visually differentiated. Grades 3-4 exhibit moderate degeneration due to dehydration of the NP and loss of distinction between the AF and NP (Figure 3). In grade 5 degeneration, the nucleus is mostly absent.

Table 1: Modified Grading System for Lumbar Disc Degeneration

Figure removed due to copyright restriction.

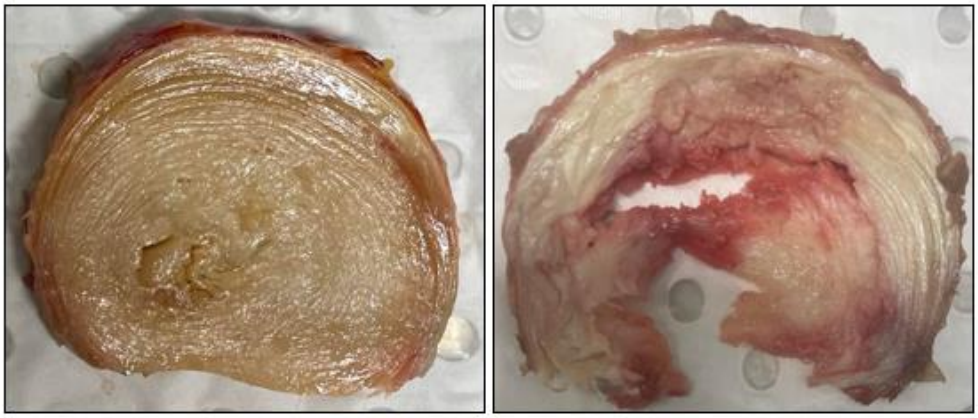

Figure 3: Non-degenerate (Grade 2) vs Degenerate discs (Grade 4)

To better understand the cause of early disc degeneration in humans, Gregory et al., 2012 conducted a peel test by initiating delamination between the two middle AF layers (Figure 4). They found that peel strength was reduced with increasing disc degeneration (Gregory et al., 2012).

Figure removed due to copyright restriction.

Figure 4: (a) Tissue sample undergoing T-peel or 180° test (b) Tissue sample after undergoing T-peel or 180° test

Microscopic analysis

Even though degeneration at tissue level has not yet been investigated, numerous methods have been used to examine the ILM's complex microstructure, across varied tissue types including, ovine, bovine and human. Animal tissues represent a suitable biochemical, biomechanical, macro- and micro-structural analogy to human discs (Wade et al., 2015, Veres et al., 2010). The findings from these studies helped to better understand the degeneration process. Bruehlmann et al., 2004 conducted the first study on the in-vivo intercellular strains of lumbar bovine discs. Under two states of biaxial strain (tension and shear), the outer annulus fibrosus of bovine discs were measured. Confocal microscopy was employed to monitor the fluorescently marked nucleus while circumferential direction was restricted at set Lagrangian strains. The structure and behaviour of the extracellular matrix surrounding the cells were found to greatly influence the intercellular mechanical environment. The intercellular strains of annular cells in situ did not match the applied

tissue strains showing it to be non-uniform and heterogenous. The interlamellar matrix in situ mechanical environment may be more complex as indicated by the increase intercellular Lagrangian strains and interlamellar shear. Other methods used to explore the ILM included light microscopy (Cassidy et al., 1989), a layer-by-layer peeling technique using stereo microscopy (Marchand and Ahmed, 1990) and histological analysis and immuno-histochemical detection (Yu et al., 2002). These techniques were used to characterize the hierarchical structure of the collagenous components of the human intervertebral disc. All of the research cited indicated that the annulus fibrosus' in situ intercellular mechanical environment was complex and non-uniform. A novel lap test done by Gregory et al., 2011 showed the ILM-lamella boundary's intricate hierarchy of interconnecting linkages by examining the ILM mechanical strength under radial stretching (Figure 5). It is therefore important to understand the impact of the surrounding matrix architecture on the intercellular mechanics with ageing and disc degeneration, where the lamellar structure is weakened.

Figure removed due to copyright restriction.

Figure 5: Lap test conducted by (Gregory, 2011) showed the ILM-lamella boundary's intricate hierarchy of interconnecting linkages by examining the ILM mechanical strength under radial stretching.

Destructive and non-destructive mechanical tests

While microstructural analysis has provided critical insights on the ILM microscopic structure, the structure-function interactions are still unanswered. Radial tensile tests of intact tissue and with enzymatic digestion (Isaacs et al., 2014) [human discs], crosslinking (Kirking et al., 2014) [bovine discs], and peel testing (Gregory et al., 2012) [rabbit discs], are a few of the studies that have been

conducted on sections of the AF to indirectly measure the mechanical properties of the ILM. Pezowicz et al., 2006 investigated both the the intra- and the inter-lamellar matrix (Figure 6).

Figure removed due to copyright restriction.

Figure 6: Intra-lamellar and inter-lamellar sections (Pezowicz, 2006)

Nuclear pressurization was used to disrupt the Intra-lamellar and inter-lamellar structures to look at the basic mechanisms behind the micromechanical characteristics of the ILM. The most basic biomechanical interpretation of disc function suggests that a compressive load applied to the intervertebral disc results in an internal increase in hydrostatic pressure in the NP which is resisted by the AF. As a result, high intradiscal pressure is associated with delamination of the AF and eventual disc degeneration. Nuclear pressurization of the NP was therefore employed to understand how annular failure might arise with increased pressurization. The disruption of the AF lamellae was found to occur at the outer and mid posterior AF, respectively. The disruption pattern showed that weaker ILM were found in the outer posterior portion of the AF making this region more susceptible to failure. Additionally, increased NP pressurization induced annular wall microdamage which varied mechanically consistently from the inner to the outer AF. Mild disturbance was seen in the outer regions, whereas severe disruption was seen in the interior AF. Despite not directly quantifying ILM mechanical properties, these findings drew significant conclusions about ILM function. For instance, increasing internal hydrostatic pressure in intact vertebra-disc-vertebra samples to 20 MPa revealed that the bovine ILM matrix in the outer AF was able to sustain the increasing nuclear pressure disruption providing a significant structural resistance in both radial and circumferential directions. These disruption patterns were in line with the discovery of Gregory et al., 2012 where a larger AF peel strength (33%), i.e., more resistant to deformation, was found in the outer AF was found compared to the inner AF.

With respect to direction of loading, earlier research has been to establish the ILM mechanical characteristics. In shear, Iatridis and ap Gwynn et al., 2004 in addition to Gregory et al., 2011 and Broom et al., 2015, found that excessive ILM stress may cause AF failure by propagating circumferential tears, thus being a cause of AF delamination. Gregory et al., 2011 used a novel lap test to look at the inter-lamellar matrix of porcine cervical discs. They found that there was high shear stress compared to tensile stress, with a mean peak strength of 0.3 N/mm at the extremities of the bonded lamellae. In addition, Fujita et al. 2020 also looked at the inter-lamellar matrix of human IVDs' 3 mm x 3 mm x 3 mm annular cubes. These cubes were subjected to shear loading along the same plane as the lamellar layers. However, rather than determining the isolated ILM, this configuration could only determine the mechanical shear properties of numerous lamella layers. Comparing Fujia's techniques to Gregory's, in order to best understand isolated ILM mechanics, lamella-ILM-lamella discs are required. The isolated ILM not only functions as a biological adhesive in the AF by holding the layers together, but it also permits some movement between the layers during spinal motion and IVD loading. It is therefore crucial to take into account a test that replicates how the tissue is loaded and fails in vivo when selecting an acceptable testing procedure.

Computational studies

Understanding ILM structure-function interactions at the tissue level is crucial for the development of engineered constructs as well as understanding how healthy and degenerative tissue functions. It was demonstrated that a computational model predictions of the overall disc behaviour are influenced by the simulated inter-lamellar connection of the annulus fibrosus. The inter-lamellar mechanical behaviour of the disc annulus under radial loading was examined using a combined experimental and computational method (Mengoni et al., 2015). The study set out to create a finite element model of the annulus fibrosus that explicitly represented inter-lamellar connection. This study showed that the lamellar connection of the annulus fibrosis affects the tissue's overall mechanical performance. However, because of the complex nature of the human lumbar spine, the finite element analysis had to be simplified and had certain limitations. In this investigation, the computational ILM radial stiffness was consistently higher than experimental tests, and it was determined that the outer AF had a larger stiffness (43–75% higher) than the inner AF. The ILM connectivity's contribution to the AF mechanical properties can be seen in the greater stiffness. Other computational studies (Schmidt et al., 2007, Wang and Wang, 2018, Johansson et al., 2017, Gunzburg et al., 1992) have simulated lumbar disc degeneration with accompanied, independently or combined, abnormalities such as: ruptures, fissures, endplate sclerosis, osteophyte formation, reduced disc height and nucleus pulposus volume, ligament failure, annulus fibre laxity, and changes

in the intervertebral disc's material properties. Few intervertebral disc morphologies could be modified in finite element (FE) models to accurately depict degenerative changes to the lumbar spine. A better understanding of understanding of the changes to the intervertebral disc and tissue characteristics is a crucial for realistic representation of disc degeneration in FE analysis.

Direct analysis of the ILM micro-mechanical properties

The most recent and only study which directly assessed the ILM micromechanical properties was conducted by Tavakoli et al., 2018. They used multiscale, biomechanical and microstructural techniques to compare the micromechanical properties between the lamellar and ILM in ovine discs. The discs were mechanically loaded in radial (tension) and circumferential (shear) using a micromechanical testing machine (BioTester, CellScale, Waterloo, ON, Canada) having a load cell capacity of $\pm$23 N. Their main finding was that the failure stress of the ILM was significantly lower than that of the lamella during both circumferential and radial loading proving that ILM is the weaker structure (Tavakoli et al., 2018). This finding strongly supports a qualitative structural analysis that suggests a biomechanical role of the ILM.

Research gaps and aims

Even though microstructural studies have helped to better understand the potential degeneration pathways, no research has evaluated the mechanical failure characteristics of the degenerated human inter-lamellar matrix (ILM). Moreover, most studies have investigated the effects of degeneration at the disc level rather than the tissue level. Many aspects of the ILM are unclear, including its mechanical function and its role in maintaining the integrity of the AF. To better understand the initiation and progression of degeneration, these properties must be investigated. From previous literature, it was observed that overall degenerated discs and healthy ILM mechanics have been investigated independently, and the micromechanical properties of the degenerated ILM are yet to be investigated. It is known that the disc enables complex, multiaxial motions, and a healthy disc is vital for normal function. However, it is known that a disc will degenerate over time and hence gaining a better understand of this complex process is important. Current research has been able to show (1) effects of degeneration and (2) techniques for understanding the micro mechanics of the disc. However, research regarding these two important factors have been done separately and are yet to be combined. Therefore, the aim of this study was ***to investigate the effect of degeneration on the micro-mechanical properties of the human ILM***.

Methodology

This work builds on methods published by Tavakoli et al. (2018). In order to achieve the aims of this project, the published methods have been further developed for degenerated and healthy human lumbar disc. This method was extensively validated on sheep lumbar discs (N=4) before moving to human disc. After pilot tests were successful, a total of 10 human lumbar discs were isolated from healthy and degenerated spines. The anterior (A) and posterolateral (PL) of each disc underwent repeatable strain rate at 3 different frequencies under tension and shear (Figure 7). All tests were performed in the Cell Scale machine. This research was carried out in the Implants & Biomechanics laboraroty at Flinders University (Tonsley).

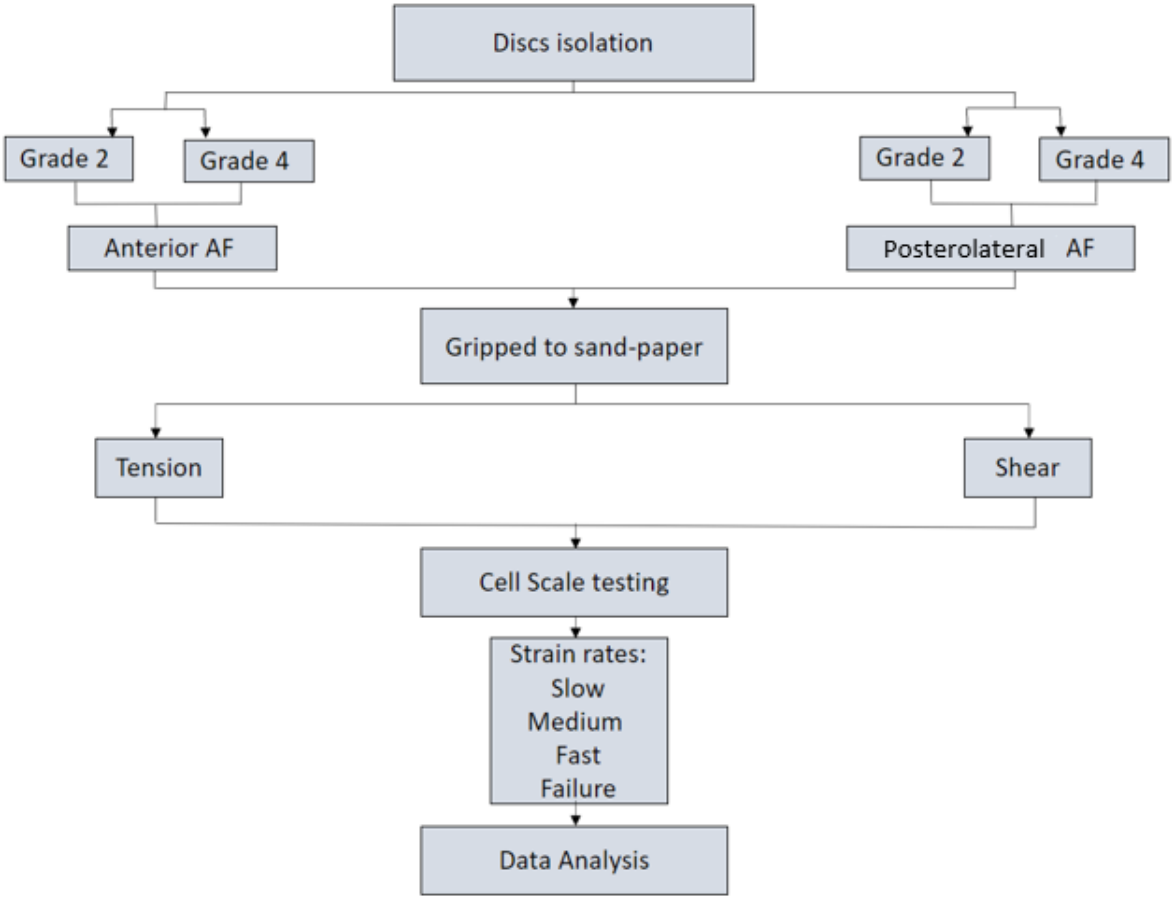

Figure 7: Study design

Sample preparation

Ten L4/L5 human lumbar discs (Grade 2: N=5) and (Grade 4: N=5), were isolated from whole lumbar spine acquired from ScienceCare (USA, Phoenix) (Appendix A). The isolated discs were sprayed with saline and stored at -20 C in cling wrap until day of testing. While frozen, a 10 mm width of the outer A and PL region of the AF, with the depth to the nucleus pulposus region was separated from each

disc (Figure 8). The outer lamellae were selected for sectioning since the individual lamellae are most distinct in the outer annulus (Marchand & Ahmed, 1990; Tsuji et al. 1993); slicing from these reduced the difficulty of obtaining sections that incorporated an area within a single lamella sufficiently large for micromechanical testing.

Figure removed due to copyright restriction.

Figure 8: Sample preparation. (a) Discs were isolated from L4/L5 region. (b)A and PL (10 mm width) were separated from the disc.

Frozen A and PL samples were then sliced using a hand microtome (Figure 9b-e). A microtome is specialized precision cutting instrument which accurately and repeatedly slices sections from a block of embedded tissue. Each sample was embedded in optimal cutting temperature compound (OCT, Tissue-Tek, Sakura, Japan) and were sliced to approximately 2 mm thickness. To achieve a uniform thickness, a platform was 3D printed (Fig 9a) so that samples could be placed on a flat surface. After securing the platform to the microtome (Fig 9b), tape was wrapped around the platform to enclose the OCT (Fig 9c). Samples were then placed on the platform and immersed in OCT (Fig 9d,e). Slices were cut in the transverse plane (Fig 9f) denoted by (*). The greater radius of curvature of the outer lamellae made it easier to cut circumferential sections that again contained a sufficient area of mono-aligned collagen structure from a single lamella.

Figure removed due to copyright restriction.

Figure 9: (a) 3D printed platform to hold specimen, (b) Mounting 3D part to microtome, (c) Tape used to prevent overflow of OCT compound, (d,e) Sample was immersed in OCT to achieve uniform thickness of 2 mm, (f) Schematic drawings of the cutting plane (*).

For mechanical testing, sliced samples were labelled and then divided into four groups for testing in the radial (tension) and circumferential (shear) directions for A and PL regions. Therefore, from each disc, a minimum of 4 slices (Anterior: N=2, Posterolateral: N=2) had to be obtained to perform all mechanical tests (Figure 10). From a total of 10 discs, 37 slices were obtained. Three specimens were excluded as there was evidence of pre-existing injury.

Figure removed due to copyright restriction.

Figure 10: The four mechanical testing groups.

Mechanical testing

To prepare the samples for the mechanical tests, a functional lamellae unit, which consisted of two adjacent lamellae and the ILM between them, was identified using a stereomicroscope (Motic, SMZ-168, China). The area enclosed by the red rectangle represents the location where samples were collected and tested (Figure 11a). Waterproof sand paper (250 grit) was bonded above and below the sample and on each edge, using cyanoacrylate adhesive. The mechanical properties of samples were measured in tension (radial) and shear (circumferential) loading directions (Figure 11b,c).

Figure removed due to copyright restriction.

Figure 11: (a) A functional lamellae unit, which consisted of two adjacent lamellae and the ILM between them. Dimension t and W represents the specimen thickness and width, respectively. Samples of the ILM and portions of two adjacent lamellae were prepared for tension (b) and shear (c) tests represented by arrows.

All samples were initially hydrated in 0.15 M phosphate buffered saline (PBS) at room temperature for 30 min and immersed in 0.15 M PBS at 37^{o}C during tests. Each sample was subjected to dynamic and failure tests using CellScale. Prior to each test, a 100 mN preload was applied, after which the test immediately started. Three cycles of dynamic loading using a triangle waveform were applied to stretch the samples to 40% of their initial length at three strain rates of 0.1%/s (slow), 1%/s (medium) and 10%/s (fast) (Figure 12) under displacement control with 2 minutes unloaded recovery period between slow, medium, fast and 5 min unloaded recovery period between fast and fail (Figure 13). It was assumed that the loading cycles did not change the biochemistry of the disc. Preload and recovery were used to minimize creep between tests. For all samples, the gripper-to-gripper distance was considered as the initial length for strain calculation after application of preload. Data frequency acquisition was set to 1, 5 and 100 Hz for slow, medium and fast strain rates, respectively. Finally, a ramp test to failure for both loading directions was performed at a strain rate of 10% at 100 Hz data acquisition.

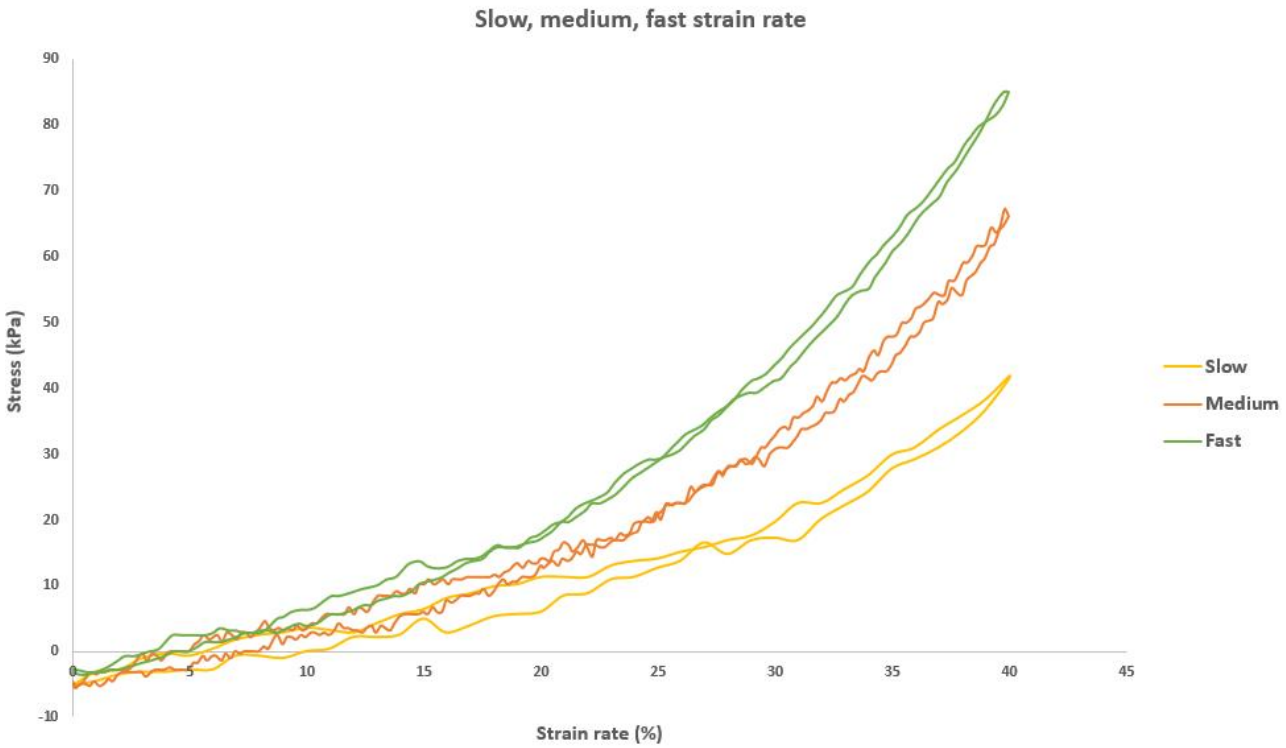

Figure 12: The viscoelastic properties (final loading cycle) of the ILM for the same sample tested of the ILM at three different strain rates of 0.1%s-1 (slow), 1%s-1 (medium) and 10%s-1 (fast).

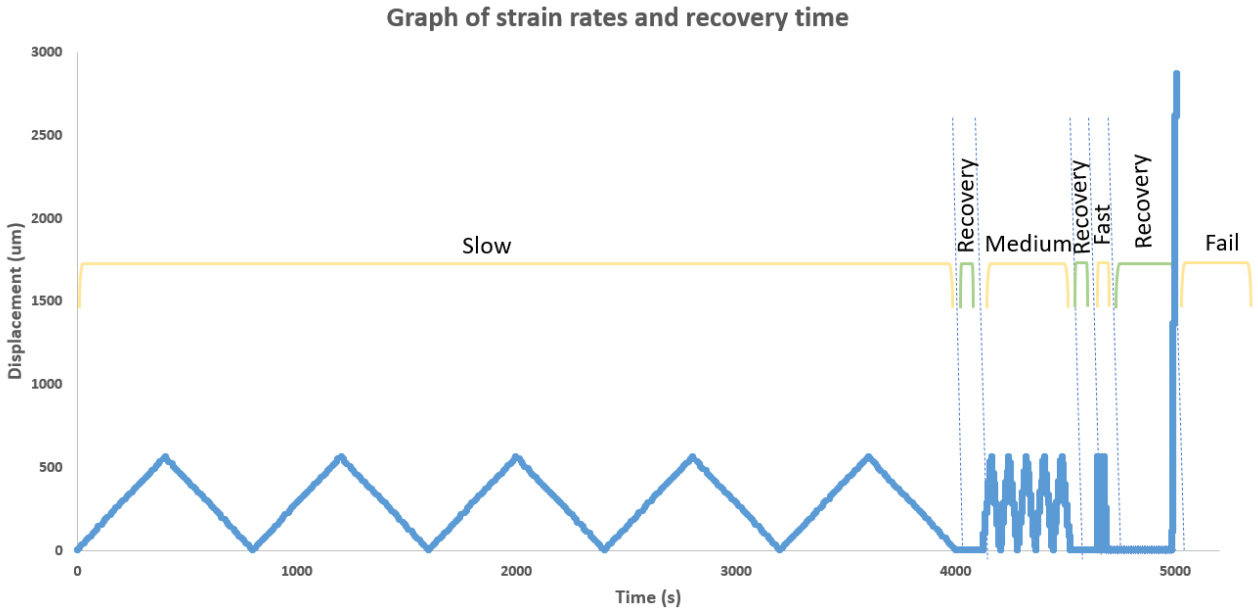

Figure 13: Two minutes unloaded recovery period between slow, medium, fast and five minutes unloaded recovery period between fast and fail.

Pilot studies

The main purpose of the pilot studies was to confirm if the protocol used by Tavakoli et al., 2018 was feasible and repeatable on human specimens. From the pilot studies, manipulation of small size (5 mm x 5 mm) ovine specimens was achieved. Specimen manipulation involved (1) cutting discs and successfully isolating a single ILM with one lamellar boundary, (2) gripping to sand paper while preventing the spread of glue on the region of interest and (3) mounting to CellScale without causing damage to the specimen. Reliable results were observed for 4 specimens and was considered competent to proceed to human testing. From the pilot testing's analysis, tools for the human specimens were also derived as explained in the next section.

Data and statistical analysis

Force and displacement were recorded from the CellScale tests from the final cycle of the dynamic tests. Force/displacement were then converted to stress and strain using appropriate specimen geometry. Specimen geometry included the cross-sectional area and initial length of the specimen and was measured using vernier calipers. Outcome measures of modulus and energy absorption (hysteresis loss coefficient) were calculated from the dynamic tests, followed by the failure test parameters of failure stress and energy absorption at failure. Failure stress was the peak stress recorded during the test. Energy absorption at failure is a measure of toughness and was calculated as the area under stress– strain curve at failure. All modulus measures were calculated as the slope of the best-fit line using linear regression, in linear regions of loading curve. Modulus was used to normalize the stiffness for comparison. Hysteresis loss coefficient was defined as the hysteresis area divided by the total area under the loading portion of the curve (Figure 14). The hysteresis area was defined as the area between the loading and unloading curves. Finally, while presenting normalized results was adopted for this study, advanced optical methods could be used to estimate the area of samples in order to calculate stress. Detailed calculations for all mechanical parameters mentioned can be found in Appendix B.

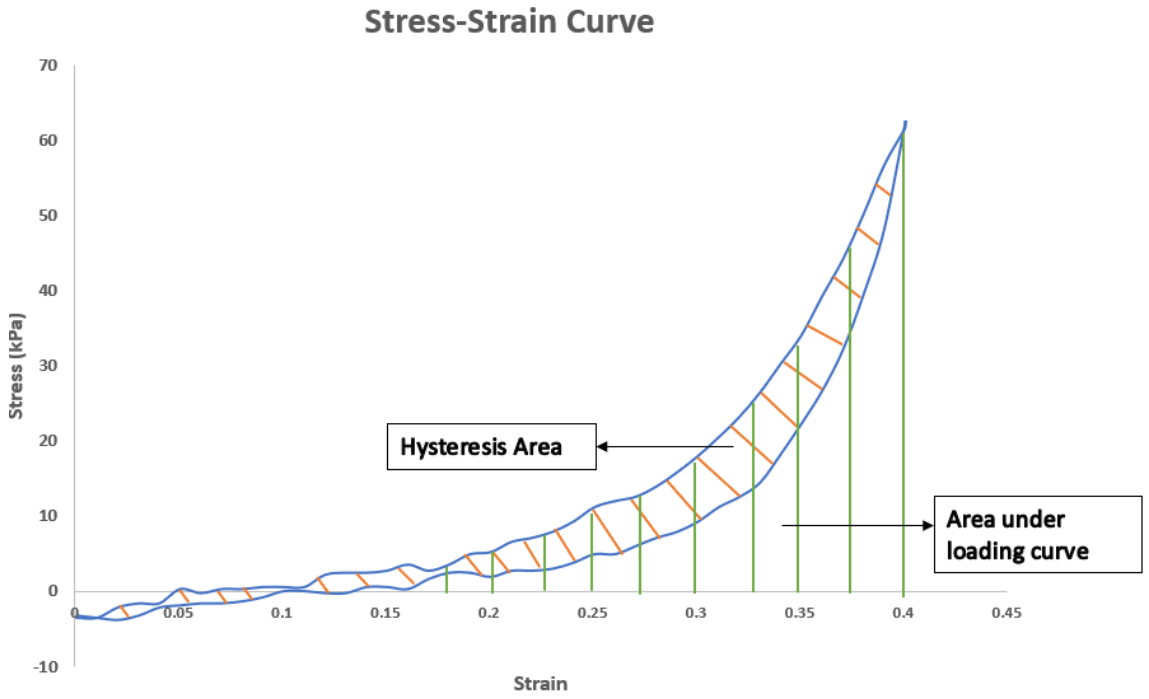

Figure 14: Hysteresis loss coefficient is the ratio of the hysteresis area (shaded orange) and the total area under the loading portion of the curve (shaded green).

For statistical analysis, separate repeated measures ANOVA were conducted (IBM SPSS Statistics for Windows, Version 22.0. Armonk, NY: IBM Corp.) for each variable of modulus and hysteresis loss coefficient having fixed factors of direction of degenerative group (Grade 2 vs Grade 4), loading direction (shear and tension), disc region (anterior vs. posterolateral) and strain rate (slow: 0.1%/s, medium: 1%/s and fast: 10%/s). For the failure tests, separate univariate ANOVA (IBM SPSS Statistics, USA) were conducted on each of failure stress and toughness, having the same fixed factors of degenerative group, loading direction and disc region. Significant effects were accepted for alpha <0.05, and when significant overall main effects were identified, post-hoc multiple comparisons were conducted using a Bonferroni adjustment on alpha.

Results

A total of 10 (Grade 2: N=5) and (Grade 4: N=5) samples were mechanically tested and analysed (all data presented in Appendix C). Three specimens were excluded from the analysis (Grade 2: N=1 and Grade 4: N=2) as there was evidence of initial pre-existing injury, thus their mechanics could not be determined. There was no indication of sample slippage during mechanical testing as identified from observation of samples during tests and analysing testing curves. Moreover, post testing analysis specimen was verified, and it was found that sandpaper fixation was constant during testing, that is, no slippage. Finally, while presenting, normalized results was adopted for this study, advanced optical methods could be used to estimate the area of samples in order to calculate stress.

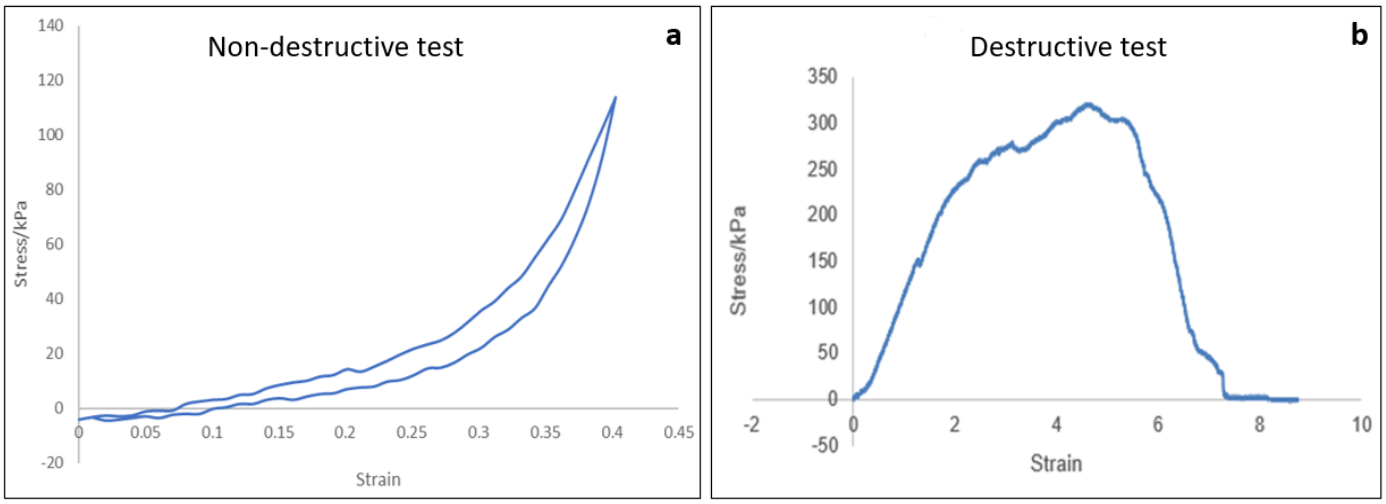

Figure 15: Mechanical testing types to verify the non-destructive viscoelastic and failure properties of the specimen (a) non-destructive and (b) failure.

Pilot testing

The presented method for isolating the ILM was successfully accomplished in 4 ovine lumbar discs. Modulus, toughness and failure were measured. It must be noted that statistical analysis was not performed for pilot test as the purpose of pilot testing was develop skills for specimen manipulation. The trends in results obtained were consistent with previous studies showing that the PL region was more prone to failure due to its low mechanical properties. In addition to agreeing with earlier research, the pilot data was essential to validate the following: Firstly, only the ILM was being mechanically investigated and not the adjacent lamellar. This was confirmed by failure tests where it was observed that the specimen failed at the ILM. Secondly, glue stayed on the grips for each sample and did not interfere with the testing region. This was confirmed visually by using colored glue and also by looking at the force-displacement graphs. Finally, there was no indication of sample

slippage during mechanical testing as identified from observation of samples during tests and analyzing testing curves. The results obtained from the pilot studies showed that the technique used to isolate the ILM was well-structured and cost efficient, without the requirement of specific knowledge and expensive equipment.

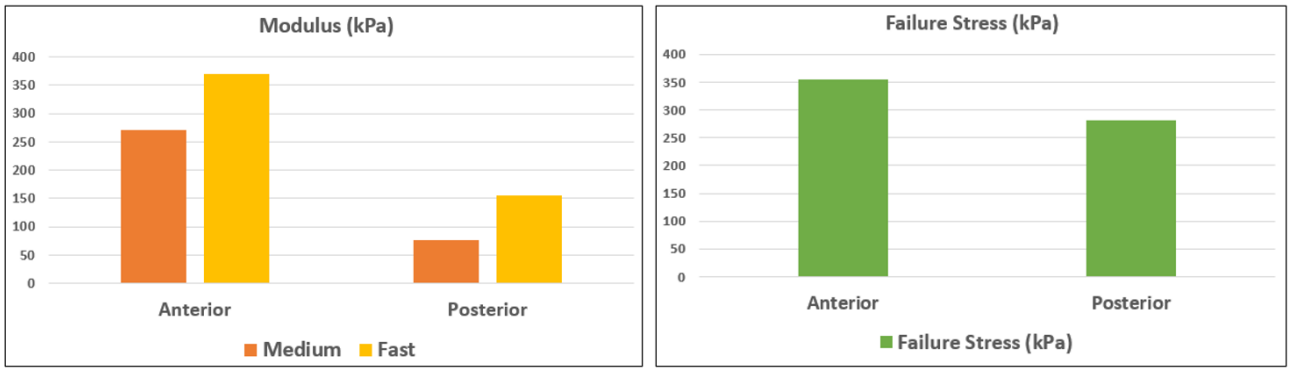

Figure 16: Mechanical parameters (modulus and failure stress) for 4 ovine lumbar discs.

Non-destructive mechanical testing

Modulus

The overall effect of strain rate on modulus was statistically significant for all examined specimens (p<0.001. However, further analysis showed no significant difference when analysing the interactions of modulus by degenerative grade (p=0.422), disc region (p=0.757) and loading direction (p=0.131). There were no significant effects when comparing modulus with combined grouping of disc region, loading directions, and degenerative grade (p=0.522). Additional analysis of possible combined grouping also failed to reveal any significant effect (p>0.522). Key statistical results for all mechanical parameters investigated are presented in Appendix D.

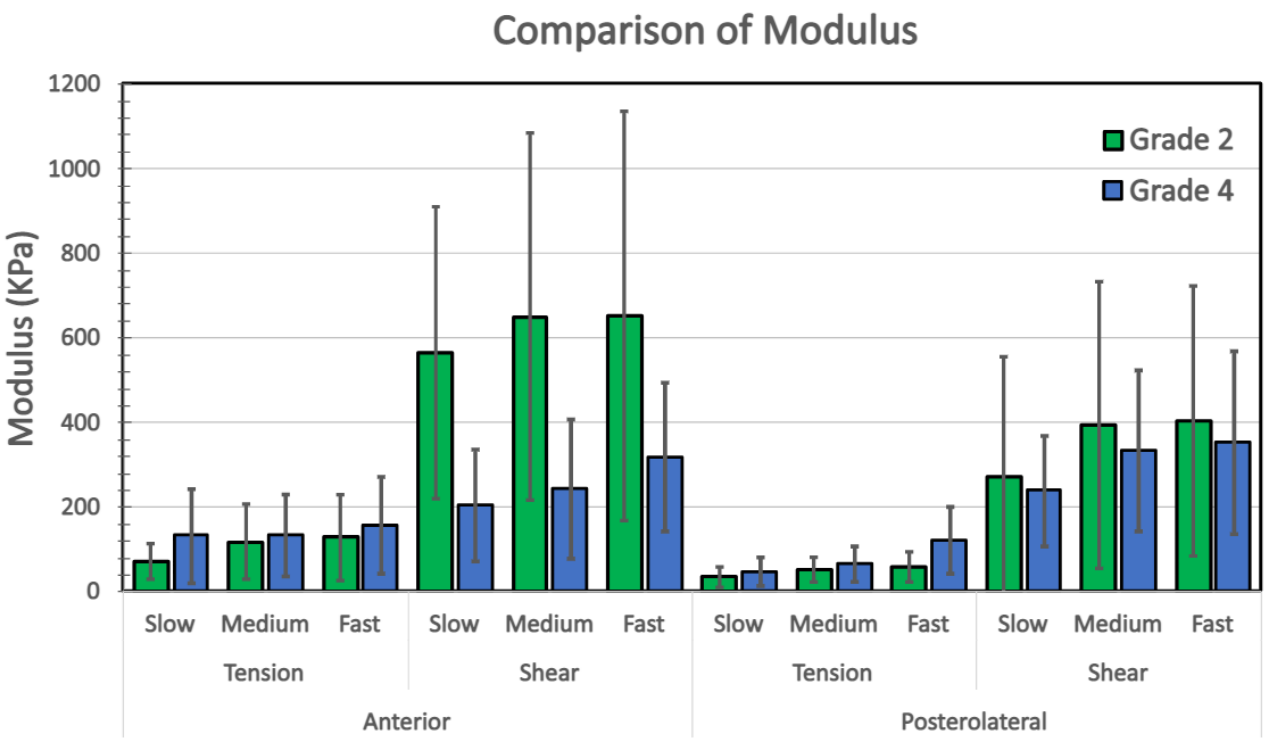

Figure 17: Mean (standard deviation) modulus (Grade 2: N=19, Grade 4: N=18)

Hysteresis loss coefficient

For each of the specimens under investigation, the overall effect of strain rate on modulus was not significant (p=0.497). Further analysis of the interactions of hysteresis loss coefficient by degenerative grade (p=0.321), disc region (p=0.652) and loading directions (p=0.308) also showed no significant changes. Additional analysis of a possible combined grouping revealed no significant effects (p>0.652).

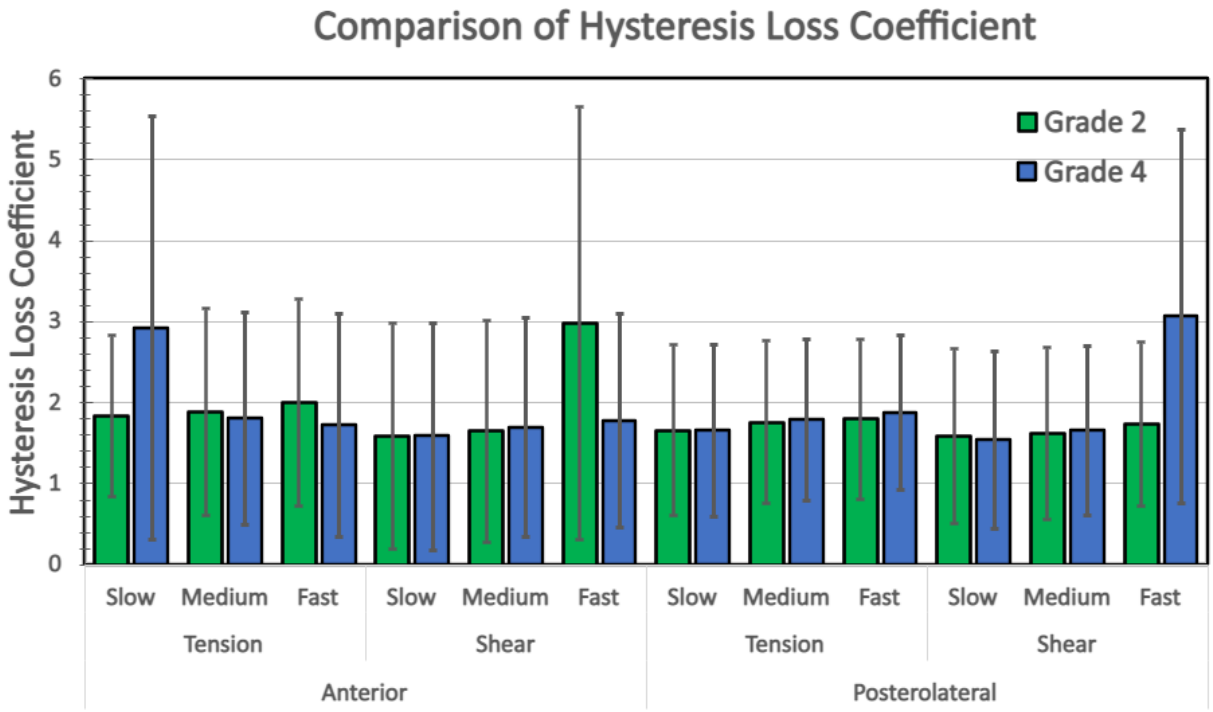

Figure 18: Mean (standard deviation) hysteresis loss coefficient (Grade 2: N=19, Grade 4: N=18)

Destructive mechanical testing

Failure tests were conducted to identify the failure mechanics of each specimen. A ramp test to failure in both loading directions was performed. Failure stress and energy absorbed, i.e., area under failure curve were calculated.

Failure stress

The overall effect of loading direction was significant ($p < 0.001$). However, further analysis showed no significant interaction across degeneration grades, region ($p=0.408$). Shear failure stress was significantly lower than tensile failure stress.

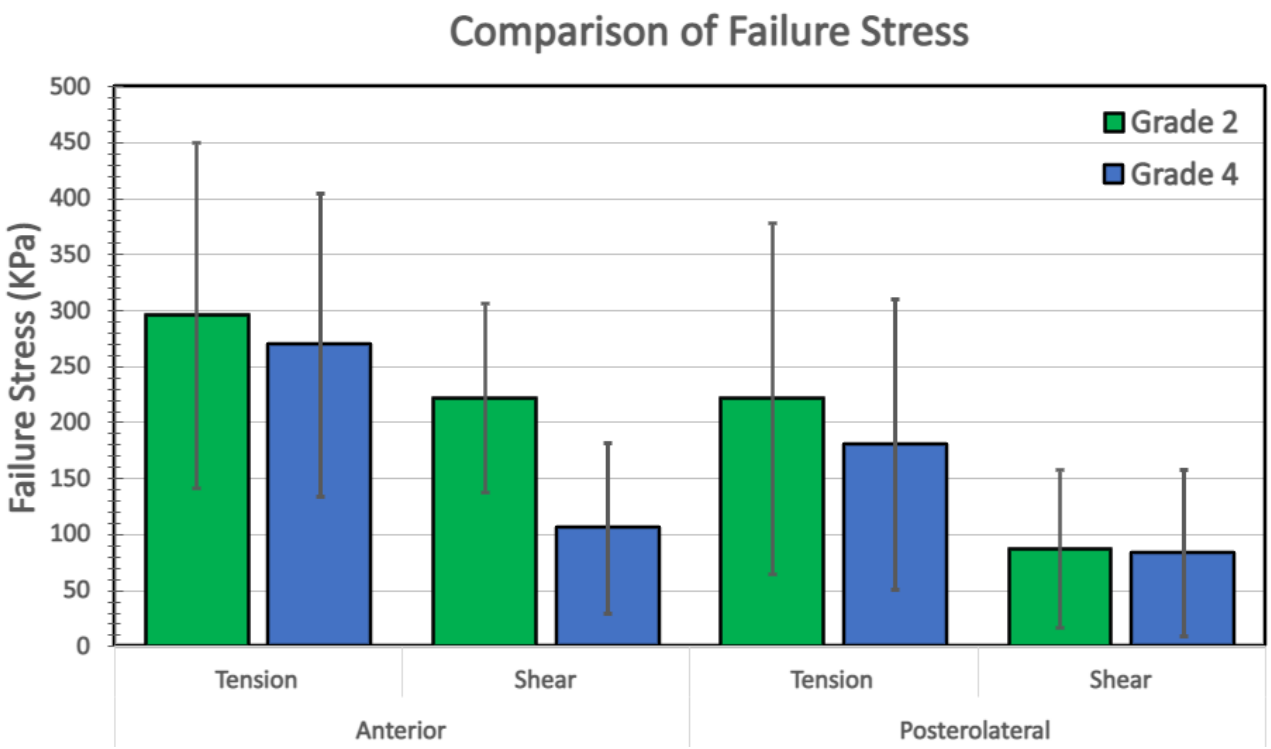

Figure 19: Mean (standard deviation) failure stress (Grade 2: N=19, Grade 4: N=18)

Energy absorption

Across all tested specimens, there was a significant effect of loading direction on energy absorption ($p<0.001$). However, further analysis showed no significant effects when analysing energy absorption by degenerative grade ($p=0.278$) and disc region ($p=0.851$). Energy absorption in tensile loading was found to be significantly larger than shear loading ($p=0.032$).

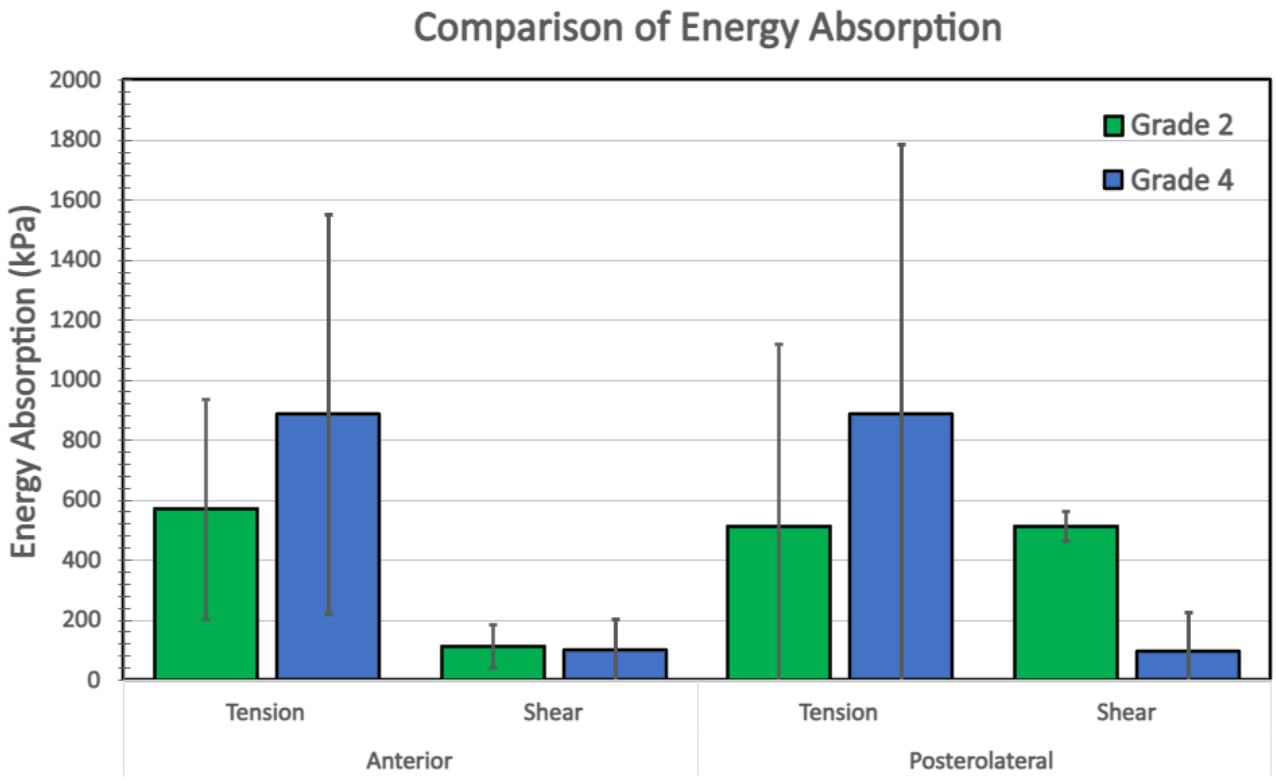

Figure 20: Mean (standard deviation) energy absorption (Grade 2: N=19, Grade 4: N=18)

Discussion

Viscoelastic behaviour was observed in all mechanical properties investigated for healthy and degenerated discs. The stress-strain cycles for the ILM were viscoelastic in nature and showed signs of hysteresis, as expected for soft tissue. While minimal significant difference was observed for the mechanical properties investigated, there were apparent trends in the data. For modulus, in both degenerative grades, shear modulus was larger than tensile modulus. In addition, shear failure stress was significantly lower than tensile failure stress. This result is consistent with what was discovered regarding shear modulus in this study. Lower shear modulus caused the specimens to be stiffer and acting like a brittle solid making this loading direction more susceptible to failure. However, this finding was not consistent with previous literature. The shear modulus of the ILM in ovine discs was found to be lower than tensile modulus and shear failure stress was higher than tensile failure stress (Tavakoli et al., 2018). This difference could be due the proteoglycans and elastic fibres recruitment in the ILM acting differently in humans and sheep. When comparing disc region, posterolateral region had a significantly lower energy absorption and failure stress compared to the anterior region in both tension and shear. This finding supports previous literature confirming that the PL regions are mostly affected than anterior region due to more delamination with degeneration (Ciapetti et al., 2012, Adams and Roughley, 2006, Fazzalari et al., 2001, Osti et al., 1992).

Modulus

From the overall results a significant change in modulus was observed with increasing strain rate. This finding is consistent with literature and shows the viscoelastic properties of the disc by showing strain rate dependent behaviour (Tavakoli and Costi., 2018). Additional grouping analyses revealed no statistically significant effects, possibly due to large variance. However, distinct trends were observed.

In both degenerative grades, the trend for shear modulus was larger than the tensile modulus. The ILM is known to offer substantial structural resistance to shear (Tavakoli et al., 2018) and this finding was confirmed in the presented data. It must be noted that Grade 2 Anterior Shear had a large shear due to two specimens bringing that average up. Since post-analysis did not show observable differences, they were not excluded. Tensile modulus increased with increasing degeneration grade. When the specimens were loaded in tension, Grade 4 specimens had a trend for being stiffer than

Grade 2 specimens. In contrasts, under shear loading, Grade 4 specimens were less stiff than Grade 2 specimens. This trend for decreasing stiffness could be a result of Grade 4 specimens acting more like a brittle solid due to breakdown of the extracellular matrix and less water content (Pham et al., 2018). The opposite trend was observed in shear loading where shear modulus decreased with increasing degeneration grade, which contradicts the proposed hypothesis, suggesting an increase in both tensile and shear modulus with increasing degeneration grade. When comparing disc regions, both tensile and shear modulus were trending lower in the posterolateral region indicating that this region is more susceptible to failure. This is because anterior regions have a more densely organised structure with complete lamellae compared to the posterolateral region with numerous incomplete lamellae (Tavakoli et al., 2016).

Hysteresis loss coefficient

Hysteresis loss coefficient is a measure of the energy absorption (damping) of the disc during loading and unloading. According to overall findings, there were no significance in hysteresis loss coefficient across degenerative grade, disc region and direction of loading. It is important to note that there was a high variance in data for the anterior region in tension and shear for slow and fast strain rate respectively and also for posterolateral shear under fast strain rate. Due to the small specimen size, the data which increased the average could not be excluded. A consistent trend was observed with increasing strain rates. Most specimens experienced a small increase in energy absorption with increasing strain rates. This is because at the slow and medium rates, the tissue had time to adjust to the change in length, minimising the degree of tensile and shear stress to which the tissue was subjected. Under the fast rate, the tissue was given less time for this rearrangement to occur. In contrast, the data for anterior region loaded in tension showed the ILM were not strain rate dependent. This discrepancy was due to two specimens increasing the average data. When the results from these two specimens were removed, the trend showed viscoelastic effect.

Failure Stress

Failure stress was defined as the maximum stress recorded during failure tests (Figure 12). At the start of the test, the specimen was not subjected to any load (rest point). When stress was applied, the specimen started to deform. The yield stress was the first deformation point. Yield stress is used to determine the specimen's ability to withstand load. If the load is greater than the yield strength, deformation will occur. The second point of deformation was at failure stress, which indicated the maximum amount of stress that the specimen can withstand before failing. Reaching this value caused the material to fail and break.

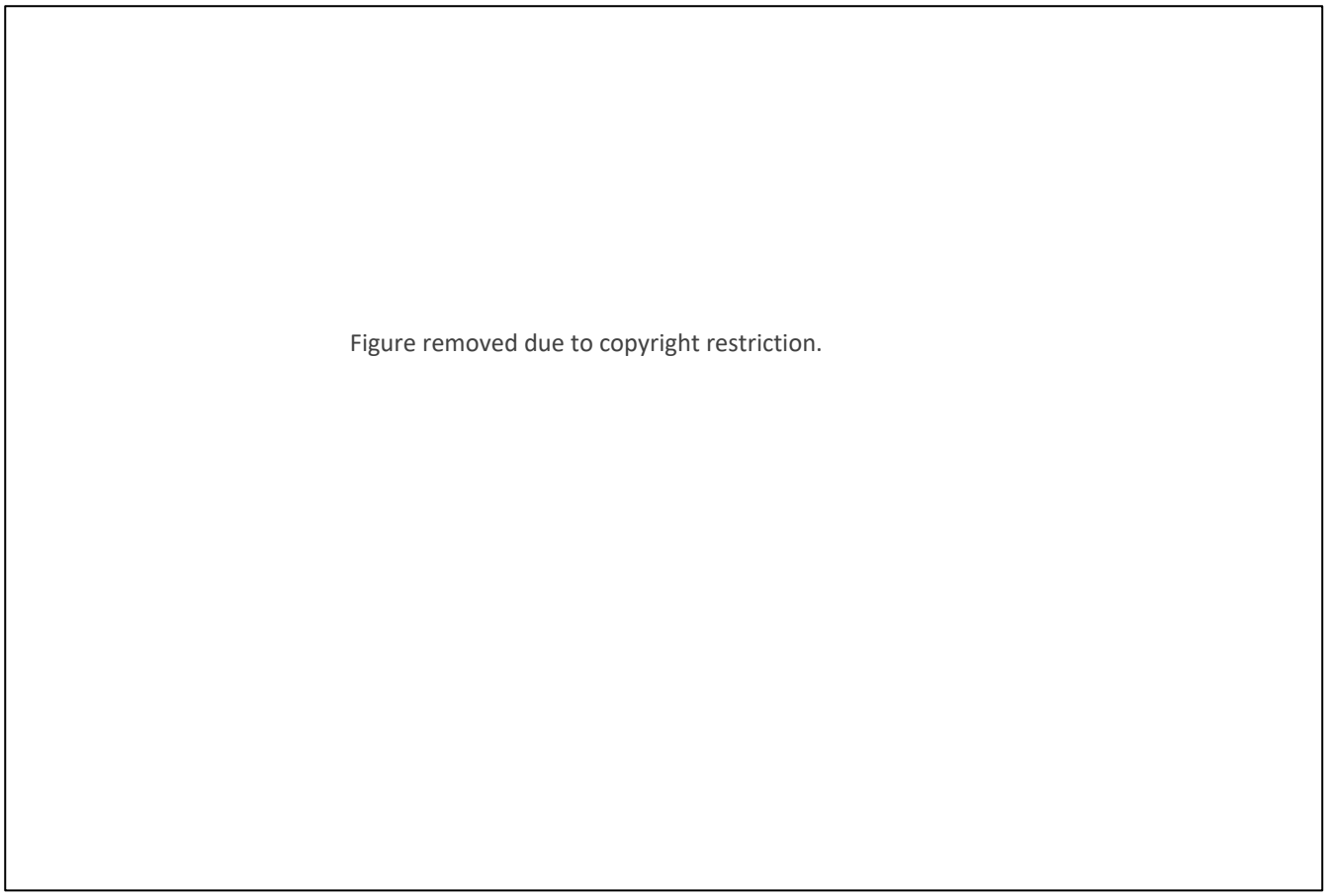

Figure 21: Mechanical failure for the ILM in tension. The images (a-d) show how the appearance of the samples changed during the mechanical failure test. (a) specimen at rest point (b) yield stress achieved, i.e, specimen starts to deform and will not return to i*nitial length (c)failure stress disrupting and separating the ILM (d) ILM failure.*

The overall effect of loading direction was significant for failure stress. However, further analysis showed no significant interaction across degeneration grades and disc region. Shear failure stress was significantly lower than tensile failure stress. This result is consistent with what was discovered regarding shear modulus. As shear modulus was found to be larger than tensile modulus for all specimens, this caused the specimens to be stiffer and acting like a brittle solid and exhibits more solid-like, as opposed to fluid-like, behaviour (Pham et al., 2018). Moreover, a lower failure stress in shear supports the understanding that discs are more vulnerable under shear stresses than tensile stresses (Ciapetti et al., 2012, Adams and Roughley, 2006, Fazzalari et al., 2001). Although no significance was determined across region, a distinct trend was observed. The trend for failure stressing the posterolateral region was lower than the anterior region. The PL region may therefore be more susceptible to failure as it was found to have lower modulus in both tension and shear. This finding can be justified by the location of PL region which is closer to the nucleus. When the nucleus is dehydrated, the point of initiation on delamination will thus be the PL region. When comparing degenerative grades, the trend for failure stress was lower in Grade 4 than Grade 2 specimens in

both tension and shear. Given that degenerated specimens are already less effective at swelling and with standing compressive loads, the trend for lower failure stress experienced was coherent. Moreover, ultrastructural studies discovered that the elastic fibre network within the ILM were likely to be recruited under tension (Tavakoli et al., 2018). However, in shear, only those fibres that were oriented in the direction of loading would likely be recruited. Therefore, due to the degenerated discs existing poor condition, shear failure stress would be expected to be lower in degenerated specimens than in healthy specimens.

Energy absorption at failure

Across all tested specimens, there was a significant effect of loading direction on energy absorption. Energy absorption in tensile loading was found to be significantly larger than shear loading. This is likely due to the high modulus found in tensile loading for Grade 4 specimens, i.e., stiffer than Grade 2 specimens. The high stiffness may be due to less water content in the NP which in turn increases the energy absorption. The opposite happened when the specimens are loaded in shear confirming the anisotropic structure of the ILM. Even though the results were not statistically significant across grades and region, clear trends were observed. In Grade 4 discs, the trend for energy absorption was higher than Grade 2 discs. It must be noted that the Grade 4 ILM in posterolateral shear demonstrated a higher capability for energy absorption in tension than in shear when one overlayed measurement was removed. When comparing disc regions, the trend for energy absorption was lower in the posterolateral region compared to the anterior region in both tension and shear. Thus, the posterolateral region appears to be less tough as the energy it can absorb before failure is low compared to the anterior region which has a larger energy absorption and can therefore absorb more energy before failure. This finding confirms that the PL regions are mostly affected than anterior region due to more delamination with degeneration.

Limitations

While this study was able to find the micromechanical behaviour of a single ILM in healthy and degenerate human AF there are some limitations to be addressed. Firstly, the sample size did not produce sufficient statistical power. The initial sample size was already small and several procedures throughout testing phase reduced it further. For example, when using the hand microtome, possible tears might develop during cutting. Therefore, samples were not collected from the first several cuts. Intact samples with minimal structural deficiency were collected. Also, the specimens were very delicate and small and damage could easily occur. To avoid that, samples were collected and handled with care to avoid structural damage. Damaged samples were not used for further analysis.

Initial tears were already present in Grade 4 specimens (Figure 22) and therefore had to be rejected. This limitation reduced specimen size. Given the variability between specimens, a larger number of samples may have resulted in the detection of additional significant differences (if they existed); thus, our findings should be interpreted with this limitation in mind.

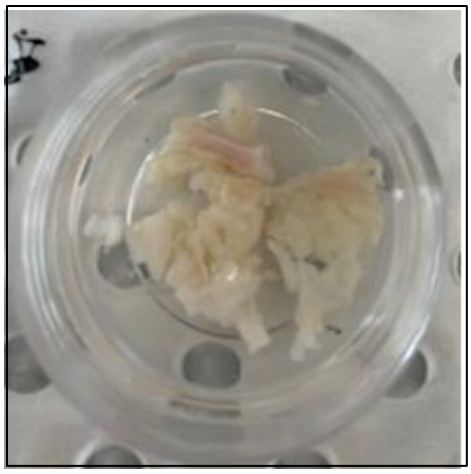

Figure 22: Existing injury in degenerated discs.

Secondly, it is inadequate to analyse disc degeneration using only in vitro experiments because these tests cannot control the different degenerative changes, being strongly dependent on the limited availability of cadavers as well as quality of cadaveric tissue Finally, few studies have been undertaken to identify the role of the ILM on mechanical properties of the AF. Lack of prior similar studies on intervertebral disc made the methodology of this study quiet challenging to compare.

Conclusion and Future work

Conclusion

For the first time, the micromechanical properties of healthy and degenerate human ILM from the outer AF were examined as a function of modulus, hysteresis loss coefficient, failure stress and toughness with respect to degenerative grade, disc region and strain rate. The goal of this study was to measure the viscoelastic and failure properties of the ILM in both tension and shear directions of loading. A strain-rate dependent response was found in the ILM during dynamic loading for all mechanical parameters investigated. While minimal significant differences were observed for modulus, there were apparent trends in the data. In both degenerative grades, the shear modulus was larger than the tensile modulus. This finding was not consistent with previous literature showing that the human ILM acts differently to ovine ILM. Moreover, Grade 4 specimens were stiffer than Grade 2 specimens under tension and the opposite trend was found in shear. This finding contradicts the proposed hypothesis suggesting that there would be an increase in both tensile and shear modulus with increasing degeneration grade. When tested to failure the ILM demonstrated a significantly lower capability for energy absorption as well as failure stress in the posterolateral region compared to the anterior region. This result supports the proposed hypothesis of the ILM maintaining the structural integrity of the AF in both healthy and degenerated discs. While the micromechanical behaviour of the ILM was achieved, a few limitations were encountered. Degenerated discs had several incomplete lamellae, thus isolating a single ILM could not be achieved. In addition, the sample size was small, and no statistical differences were found amongst degenerative grade, direction of loading, or disc region across all mechanical parameters investigated. Despite the limitations encountered and insufficient statistical power, the results obtained in this study enhanced our knowledge about the mechanics of the ILM in healthy and degenerated discs. The findings of this research can be used for a better understanding of the initiation and progression of delamination that result in degeneration on AF structural integrity.

Future work

Additional research is needed to further investigate the micromechanical properties of the ILM. Based on the findings of this thesis, a disparity in tensile modulus was observed. The results obtained were not consistent with previous literature. While ovine discs were thought to be a suitable biomechanical, macro- and micro-structural analogy for human discs, an opposite outcome for modulus was observed in humans. As a result, further investigation is required. Ultrastructural data such as visualizing the ILM under high magnification could potentially reveal the difference in disc architecture in humans compared to sheep when loaded under tension and shear. Moreover, Grade 4 discs had several incomplete lamellae. It was therefore challenging to isolate a single ILM with one lamellar boundary. Most of those specimens failed at the lamellar-sand paper boundary rather than at the ILM. Thus, an improved technique for gripping degenerated specimens must be derived. Tissue strain was measured based on the gripper-to-gripper distance of the CellScale. For a better representation of tissue strain, speckles (acting as points) could be added to the specimen and the distance from initial to the final points can be calculated using non-contact strain analysis software already integrated into the CellScale. Although this study allowed a direct analysis of the ILM, future studies would benefit from testing a larger number of samples as no statistical difference were found amongst degenerative grade, direction of loading, disc region across all mechanical parameters investigated. Further experimental evidence with a larger sample size is therefore required.

REFERENCES

ADAMS, M. A. & ROUGHLEY, P. J. 2006. What is intervertebral disc degeneration, and what causes it? Spine, 31, 2151-2161.

AMIN, D., MOAWAD, C. & COSTI, J. 2019. New findings confirm regional internal disc strain changes during simulation of repetitive lifting motions. Annals of biomedical engineering, 47, 1378-1390.

BONNEVIE, E. D., GULLBRAND, S. E., ASHINSKY, B. G., TSINMAN, T. K., ELLIOTT, D. M., CHAO, P.-H. G., SMITH, H. E. & MAUCK, R. L. 2019. Aberrant mechanosensing in injured intervertebral discs as a result of boundary-constraint disruption and residual-strain loss. Nature biomedical engineering, 3, 998-1008.

BRUEHLMANN, S. B., HULME, P. A. & DUNCAN, N. A. 2004. In situ intercellular mechanics of the bovine outer annulus fibrosus subjected to biaxial strains. Journal of biomechanics, 37, 223-231.

CASSIDY, J., HILTNER, A. & BAER, E. 1989. Hierarchical structure of the intervertebral disc. Connective tissue research, 23, 75-88.

CIAPETTI, G., GRANCHI, D., DEVESCOVI, V., LEONARDI, E., GREGGI, T., DI SILVESTRE, M. & BALDINI, N. 2012. Ex vivo observation of human intervertebral disc tissue and cells isolated from degenerated intervertebral discs. European Spine Journal, 21, 10-19.

COSTI, J. J., STOKES, I. A., GARDNER-MORSE, M., LAIBLE, J., SCOFFONE, H. M. & IATRIDIS, J. 2007. Direct measurement of intervertebral disc maximum shear strain in six degrees of freedom: motions that place disc tissue at risk of injury. Journal of biomechanics, 40, 2457-2466.

DEYO, R. A., GRAY, D. T., KREUTER, W., MIRZA, S. & MARTIN, B. I. 2005. United States trends in lumbar fusion surgery for degenerative conditions. Spine, 30, 1441-1445.

FAZZALARI, N. L., COSTI, J. J., HEARN, T. C., FRASER, R. D., VERNON-ROBERTS, B., HUTCHINSON, J., MANTHEY, B. A., PARKINSON, I. H. & SINCLAIR, C. 2001. Mechanical and pathologic consequences of induced concentric anular tears in an ovine model. Spine, 26, 2575-2581.

FUJITA, Y., WAGNER, D., BIVIJI, A., DUNCAN, N. & LOTZ, J. 2000. Anisotropic shear behavior of the annulus fibrosus: effect of harvest site and tissue prestrain. Medical engineering & physics, 22, 349-357.

GREGORY, D. E., BAE, W. C., SAH, R. L. & MASUDA, K. 2012. Anular delamination strength of human lumbar intervertebral disc. European Spine Journal, 21, 1716-1723.

GREGORY, D. E., VELDHUIS, J. H., HORST, C., BRODLAND, G. W. & CALLAGHAN, J. P. 2011. Novel lap test determines the mechanics of delamination between annular lamellae of the intervertebral disc. Journal of biomechanics, 44, 97-102.

GUNZBURG, R., PARKINSON, R., MOORE, R., CANTRAINE, F., HUTTON, W., VERNON-ROBERTS, B. & FRASER, R. 1992. A cadaveric study comparing discography, magnetic resonance imaging, histology, and mechanical behavior of the human lumbar disc. Spine, 17, 417-426.

IATRIDIS, J. C. & AP GWYNN, I. 2004. Mechanisms for mechanical damage in the intervertebral disc annulus fibrosus. Journal of biomechanics, 37, 1165-1175.

ISAACS, J. L., VRESILOVIC, E., SARKAR, S. & MARCOLONGO, M. 2014. Role of biomolecules on annulus fibrosus micromechanics: effect of enzymatic digestion on elastic and failure properties. Journal of the Mechanical Behavior of Biomedical Materials, 40, 75-84.

JACOBS, N. T., SMITH, L. J., HAN, W. M., MORELLI, J., YODER, J. H. & ELLIOTT, D. M. 2011. Effect of orientation and targeted extracellular matrix degradation on the shear mechanical properties of the annulus fibrosus. Journal of the mechanical behavior of biomedical materials, 4, 1611-1619.

JOHANSSON, M., JENSEN STOCHKENDAHL, M., HARTVIGSEN, J., BOYLE, E. & CASSIDY, J. 2017. Incidence and prognosis of mid-back pain in the general population: a systematic review. European Journal of Pain, 21, 20-28.

KIRKING, B., HEDMAN, T. & CRISCIONE, J. 2014. Changes in the interfacial shear resistance of disc annulus fibrosus from genipin crosslinking. Journal of biomechanics, 47, 293-296.

MARCHAND, F. & AHMED, A. M. 1990. Investigation of the laminate structure of lumbar disc anulus fibrosus. Spine, 15, 402-410.

MCNALLY, D. & ADAMS, M. A. 1992. Internal intervertebral disc mechanics as revealed by stress profilometry. Spine, 17, 66-73.

MENGONI, M., LUXMOORE, B. J., WIJAYATHUNGA, V. N., JONES, A. C., BROOM, N. D. & WILCOX, R. K. 2015. Derivation of inter-lamellar behaviour of the intervertebral disc annulus. Journal of the mechanical behavior of biomedical materials, 48, 164-172.

NACHEMSON, A. 1965. In vivo discometry in lumbar discs with irregular nucleograms some differences in stress distribution between normal and moderately degenerated discs. Acta Orthopaedica Scandinavica, 36, 418-434.

PEZOWICZ, C. A., SCHECHTMAN, H., ROBERTSON, P. A. & BROOM, N. D. 2006. Mechanisms of anular failure resulting from excessive intradiscal pressure: a microstructural-micromechanical investigation. Spine, 31, 2891-2903.

PFIRRMANN, C. W., METZDORF, A., ZANETTI, M., HODLER, J. & BOOS, N. 2001. Magnetic resonance classification of lumbar intervertebral disc degeneration. spine, 26, 1873-1878.

PHAM, D. T., SHAPTER, J. G. & COSTI, J. J. 2018. Tensile behaviour of individual fibre bundles in the human lumbar anulus fibrosus. Journal of biomechanics, 67, 24-31.

SCHMIDT, H., KETTLER, A., ROHLMANN, A., CLAES, L. & WILKE, H.-J. 2007. The risk of disc prolapses with complex loading in different degrees of disc degeneration–a finite element analysis. Clinical biomechanics, 22, 988-998.

SCHOLLUM, M. L., ROBERTSON, P. A. & BROOM, N. D. 2008. ISSLS prize winner: microstructure and mechanical disruption of the lumbar disc annulus: part I: a microscopic investigation of the translamellar bridging network. Spine, 33, 2702-2710.

SKRZYPIEC, D. M., POLLINTINE, P., PRZYBYLA, A., DOLAN, P. & ADAMS, M. A. 2007. The internal mechanical properties of cervical intervertebral discs as revealed by stress profilometry. European Spine Journal, 16, 1701-1709.

STANDARD, A. 2008. Standard test method for peel resistance of adhesives (T-Peel Test). Active Standard ASTMD1876, 15.

STOKES, I. A. & IATRIDIS, J. C. 2004. Mechanical conditions that accelerate intervertebral disc degeneration: overload versus immobilization. Spine, 29, 2724.

TAVAKOLI, J., AMIN, D. B., FREEMAN, B. J. & COSTI, J. J. 2018. The biomechanics of the inter-lamellar matrix and the lamellae during progression to lumbar disc herniation: which is the weakest structure? Annals of biomedical engineering, 46, 1280-1291.

TAVAKOLI, J. & COSTI, J. J. 2018. New insights into the viscoelastic and failure mechanical properties of the elastic fiber network of the inter-lamellar matrix in the annulus fibrosus of the disc. Acta Biomaterialia, 77, 292-300.

TAVAKOLI, J., ELLIOTT, D. M. & COSTI, J. J. 2016. Structure and mechanical function of the inter-lamellar matrix of the annulus fibrosus in the disc. Journal of Orthopaedic Research, 34, 1307-1315.

TSANTRIZOS, A., ITO, K., AEBI, M. & STEFFEN, T. 2005. Internal strains in healthy and degenerated lumbar intervertebral discs. Spine, 30, 2129-2137.

WANG, K. & WANG, H. 2018. The biomechanical influence of anterior vertebral body osteophytes on the lumbar spine: A finite element study. The Spine Journal, 18, 2288-2296.

WALKER, B. F. 2000. The prevalence of low back pain: a systematic review of the literature from 1966 to 1998. Clinical Spine Surgery, 13, 205-217.

WARIS, E., ESKELIN, M., HERMUNEN, H., KIVILUOTO, O. & PAAJANEN, H. 2007. Disc degeneration in low back pain: a 17-year follow-up study using magnetic resonance imaging. Spine, 32, 681-684.

WILKE, H.-J., ROHLMANN, F., NEIDLINGER-WILKE, C., WERNER, K., CLAES, L. & KETTLER, A. 2006. Validity and interobserver agreement of a new radiographic grading system for intervertebral disc degeneration: Part I. Lumbar spine. European Spine Journal, 15, 720-730.

YU, J., PETER, C., ROBERTS, S. & URBAN, J. P. 2002. Elastic fibre organization in the intervertebral discs of the bovine tail. Journal of anatomy, 201, 465-475.

Appendices

APPENDIX A

List of the specimens used for the study.

The code name was used for identifying different specimens.

Specimen Number	Age	Gender	Weight	BMI	Levels	Grade
W10/W20	59	M	180	29	L4-5	2
W24/W25	58	M	150	20.3	L4-5	2
W29/W36	31	M	300	43	L4-5	2
W37/W39	55	M	120	17.2	L4-5	2
W12/W13	49	F	229	41.9	L4-5	2
GL1911447	34	M	173.8	22	L4-5	4
GL1911794	51	M	105	15	L4-5	4
GL1911471	65	M	200	30.4	L4-5	4
GL1912463	54	M	175	25.1	L4-5	4
GL1911813	61	F	100	18.3	L4-5	4

Appendix B

Calculation of all mechanical parameters

Modulus

Strain, $\varepsilon = \frac{\Delta L}{L_o}$, where ΔL is the change in length (original length – final length) and L_o Is the original length.

Stress, $\sigma = \frac{F}{A}$, where *F* is the resultant force after displacement is applied, expressed in Newtons (N). *A* is the cross-sectional area of the sample, expressed in square metres (mm2). Stress is therefore expressed in kPa

From stress and strain, modulus is the the gradient of the stress-strain relationship.
Modulus, E= $\frac{\sigma}{\varepsilon}$

Hysteresis Loss Coefficient

Hysteresis loss coefficient is the ratio between the loading and unloading area under graph and area under loading graph. Area between loading and unloading curve was calculated using approximation of numerical integration; Area under graph = (xi + xi+1)/2*(yi+1 – yi). The total area under the curve is the sum of the incremental areas. To differentiate between loading and unloading curves, for compression test, *MAX(stress)* was found

using excel and for rotation, *MAX(rotation)* was found. *[Hysteresis=SUM(Area loading)-SUM(area unloading)]* The sums were recorded separately in 2 different columns and the hysteresis loss coefficient was calculated.

Failure Stress

Defined as the maximum stress reached and command *MAX(stress) was used in Excel to find the corresponded value.*

Energy Absorption at failure

Area was calculated using approximation of numerical integration; Area under graph = (xi + xi+1)/2*(yi+1 – yi). The total area under the curve is the sum of the incremental areas.

Calculation Template

Temperat	XSize_um	YSize_um	XDisplace	YDisplace	XForce_m	YForce_m	Loading area	Cross area/mm2	y0/um	Strain	Stress
30.1	4700	1662	0	0	0	-40	-0.003569948	25.54	1020	-2.35294E-07	-1.56617
30.1	4700	1665	0	3	1.4	-22	-0.005067023			0.002940941	-0.86139
30.1	4700	1671	0	9	1.4	-22	-0.003358822			0.008823294	-0.86139
30.1	4700	1676	0	14	1.4	-13	-0.000806117			0.013725255	-0.50901
30.1	4700	1682	0	20	0	6	0.001381915			0.019607608	0.234926
30.1	4700	1688	0	26	0	6	0.000191933			0.025489961	0.234926
30.1	4700	1693	0	31	0	-4	-0.001957713			0.030391922	-0.15662
30.1	4700	1699	0	37	0	-13	-0.00299415			0.036274275	-0.50901
30.1	4700	1705	0	43	-1.4	-13	-0.001631428			0.042156627	-0.50901
30.1	4700	1710	0	48	0	-4	0.000191933			0.047058588	-0.15662
30.1	4700	1715	0	53	0	6	0.00282141			0.051960549	0.234926
30.1	4700	1722	0	60	0	15	0.00287899			0.058823294	0.587314
30.1	4700	1727	0	65	0	15	0.00287899			0.063725255	0.587314
30.1	4700	1732	0	70	0	15	0.004030586			0.068627216	0.587314
30.1	4700	1739	0	77	-1.4	15	0.003742687			0.075489961	0.587314
30.1	4700	1744	0	82	-1.4	24	0.004606384			0.080391922	0.939702
30.1	4700	1749	0	87	-1.4	24	0.006448938			0.085293882	0.939702
30.1	4700	1756	0	94	0	24	0.004606384			0.092156627	0.939702
30.1	4700	1761	0	99	0	24	0.004606384			0.097058588	0.939702
30.1	4700	1766	0	104	0	24	0.005527661			0.101960549	0.939702
30.1	4700	1772	0	110	0	24	0.005527661			0.107842902	0.939702
30.1	4700	1778	0	116	0	24	0.004606384			0.113725255	0.939702
30.1	4700	1783	0	121	0	24	0.006564098			0.118627216	0.939702
30.1	4700	1789	0	127	-1.4	33	0.006333779			0.124509569	1.292091
30.1	4700	1794	0	132	-1.4	33	0.006333779			0.129411529	1.292091
30.1	4700	1799	0	137	0	33	0.00886729			0.13431349	1.292091
30.1	4700	1806	0	144	0	33	0.007197476			0.141176235	1.292091
30.1	4700	1811	0	149	-1.4	42	0.009788567			0.146078196	1.644479
30.1	4700	1816	0	154	-1.4	60	0.017331521			0.150980157	2.349256
30.1	4700	1823	0	161	0	69	0.014107052			0.157842902	2.701644
30.1	4700	1828	0	166	0	78	0.015834447			0.162744863	3.054033
30.1	4700	1833	0	171	0	87	0.023377401			0.167646824	3.406421
30.1	4700	1840	0	178	0	87	0.016698144			0.174509569	3.406421

Max force/mN	**954**
Max Stress/kPa	**37.35317**
y1	18.67659
y2	33.61785
Modulus	**105.7397**
Area Loading	**6.913147**
Unloading	-5.76351
Hysteresis area	**12.67666**
Energy absorbed	**0.545345**

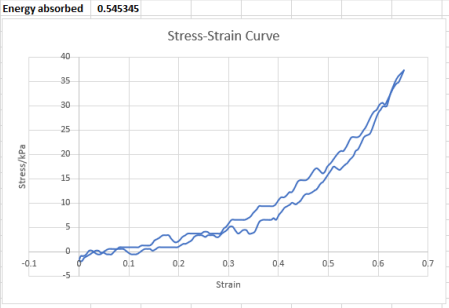

Appendix C

Data obtained for each disc and their corresponding average.

GRADE2 W10/W20																
	Tension								Shear							
	Anterior				Posterior-tears				Anterior				Posterior-tears			
	Slow	Medium	Fast	Fail	Slow	Medium	Fast	Fail	Slow	Medium	Fast	Fail	Slow	Medium	Fast	Fail
Maxforce/mN	294	465	673	4143	302	519	699	1964	3404	4000	4434	6304	1760	811	766	956
MaxStress/kPa	9.858494	15.59252	22.56723	238.9243	9.994539	17.17605	23.13306	64.9976	113.9643	133.9181	148.4482	211.0549	50.933	23.46969	22.16743	23.50393
Modulus	42.45231	62.25284	63.3834		13.64413	43.60025	45.52399		893	1058.774	1141.505		162.0174	163.6489	147.6703	
Hysteresisloss	2.370919	4.089696	6.723672		2.521208	5.868673	8.586357		15.22992	20.40801	**2.980402**		7.292534	3.9465	3.504602	
Energy Absorbed	1.436772	2.272322	3.591507		1.555997	3.341295	4.643459		9.843172	11.98293	2.876026		4.453419	2.454308	2.032636	

GRADE2 W24/W25																
	Tension								Shear							
	Anterior				Posterior-tears				Anterior				Posterior			
	Slow	Medium	Fast	Fail	Slow	Medium	Fast	Fail	Slow	Medium	Fast	Fail	Slow	Medium	Fast	Fail
Maxforce/mN	1758	2264	2761	6971					3539	4000	5509	6720	1176	1600	1799	3118
MaxStress/kPa	60.36404	77.73844	93.71839	340.7036					118.4595	133.89203	184.4004	224.9357	36.57444	49.76115	55.95019	96.97203
Modulus	111.2695	252.9564	291.7524						826.2718	1038.095	1099.289		242.072	280.7857	356.0212	
Hysteresisloss	12.10153	16.25131	20.64446						15.49765	20.77227	30.3739		3.854756	6.152039	6.752863	
Energy Absorbed	6.691356	8.816347	10.94788						9.125407	12.21656	17.50325		2.422993	3.642776	3.848323	

GRADE2 W29/W36																
	Tension								Shear							
	Anterior				Posterior				Anterior				Posterior			
	Slow	Medium	Fast	Fail -Slip	Slow	Medium	Fast	Fail	Slow	Medium	Fast	Fail	Slow	Medium	Fast	Fail
Maxforce/mN	943	1242	1458	11212	298	515	804	7481	2067	1940	1588	2437	2417	3492	3655	5019
MaxStress/kPa	39.52387	52.05583	61.10902	469.9275	12.7551	22.04321	34.02167	320.2044	62.43657	58.60036	47.96772	73.61292	95	137.2642	158.706	197.2877
Modulus	82.21649	144.4022	156.1621		56.34698	73.60967	87.63527		423.107	358.6926	189.8322		779.7334	1014.899	830.9146	
Hysteresisloss	11.40012	15.13496	18.43747		2.445085	5.148382	9.164466		7.2842	9.204114	8.264955		7.046194	13.37397	26.85902	
Energy Absorbed	6.328946	8.184271	9.913857		1.560046	2.874007	5.171307		4.339219	5.522462	4.735076		4.812878	8.399306	15.33462	

GRADE2 W37/W39																
	Tension								Shear							
	Anterior				Posterior-initialtears				Anterior				Posterior			
	Slow	Medium	Fast	Fail	Slow	Medium	Fast	Fail	Slow	Medium	Fast	Fail	Slow	Medium	Fast	Fail
Maxforce/mN	352	451	514	1915				1070	2900	3614	4165	5213	696	714	777	1129
MaxStress/kPa	15.85443	20.31349	23.15107	206.25349				34.04997	71.87469	89.57073	103.2269	129.201	20.16737	20.68894	22.51443	32.71402
Modulus	53.32017	85.29284	71.7365						473.2837	583.9287	576.1084		63.665	92.92931	96.31539	
Hysteresisloss	4.706771	6.167906	7.202271						6.65544	11.44197	13.05747		3.935694	4.442636	4.48054	
Energy Absorbed	2.741635	3.377087	3.899429						4.385382	6.966343	7.537845		2.421374	2.698885	2.611939	

GRADE2 W12/W13																
	Tension								Shear							
	Anterior				Posterior				Anterior				Posterior			
	Slow	Medium	Fast	Fail	Slow	Medium	Fast	Fail	Slow	Medium	Fast	Fail	Slow	Medium	Fast	Fail
Maxforce/mN		662	734	3074	508	517	553	6444	1574	2034	2052	2342	930	3492	3665	5019
MaxStress/kPa		26.4377	29.3131	122.7936	22.02414	22.41433	23.9751	279.3771	59.93907	77.45621	78.14166	89.18507	40.38211	151.6283	158.706	217.9331
Modulus		45.79706	65.75651		37.53969	40.3776	44.30301		207.5705	214.5898	253.5202		112.5237	519.6713	591.6981	84.2884
Hysteresisloss		13.1385	9.748791		60823482	7.553907	7.617404		7.202882	10.96433	10.79937		6.446594	25.38677	26.85902	
Energy Absorbed		7.432798	5.742094		3.760695	4.094309	4.110584		4.898861	7.085375	6.64507		3.840973	15.68157	15.33462	

GRADE4 GL1911447																
	Tension								Shear							
	Anterior				Posterior				Anterior				Posterior			
	Slow	Medium	Fast	Fail	Slow	Medium	Fast	Fail	Slow	Medium	Fast	Fail	Slow	Medium	Fast	Fail
Maxforce/mN	2179	1653	1988	6370	1076	1726	2187	7481	642	669	723	868	4255	5195	4075	5412
MaxStress/kPa	79.64181	70.12409	84.33556	270.2301	41.81824	67.08019	84.99674	290.7456	41.36598	43.10567	46.58505	55.92784	202.4263	247.1456	193.863	257.4691
Modulus	295.2332	166.9207	286.0159		71.41625	76.78481	179.042		144.2322	144.371	188.6386		1419.109	1309.904	718.701	
Hysteresisloss	15.63869	16.56516	20.46695		9.415511	17.88355	24.41715		6.280088	7.167635	7.582908		20.69143	37.16421	35.27799	
Energy Absorbed	9.247192	9.010981	10.67341		5.656754	9.733055	12.68817		3.565083	3.991657	4.079484					

GRADE4 GL1911471																
	Tension								Shear							
	Anterior-good s,m,f graphs				Posterior				Anterior- good s,m,f gaph				Posterior			
	Slow	Medium	Fast	Fail	Slow	Medium	Fast	Fail	Slow	Medium	Fast	Fail	Slow	Medium	Fast	Fail
Maxforce/mN	1644	2177	2412	3424	565	891	1333	2201	2576	3832	4545	6307	867	651	596	1003
MaxStress/kPa	80.17322	106.1661	117.6264	166.9788	28.25	44.55	66.65	110.05	126.9409	188.8345	223.97	55.92784	38.04834	28.56917	26.15549	44.01671
Modulus	193.8486	281.4897	263.7709		77.60698	106.268	168.6368		397.3878	490.8692	538.3521		109.9565	111.4619	113.6563	
Hysteresisloss	17.17168	30.18774	35.93109		5.142761	11.18868	20.97192		20.49741	36.91219	44.98753		5.108032	4.751626	4.558188	
Energy Absorbed	9.972655	16.90395	19.37825		3.49431	6.566273	11.71069		12.2325	21.25935	25.05405		3.391162	2.899184	2.613995	

GRADE4 GL1912463																
	Tension								Shear							
	Anterior				Posterior				Anterior -goos graph for s,m,f				Posterior			
	Slow	Medium	Fast	Fail	Slow	Medium	Fast	Fail	Slow	Medium	Fast	Fail	Slow	Medium	Fast	Fail
Maxforce/mN	354	436	589	5494					1727	2115	2468	6398	1098	1559	1749	5884
MaxStress/kPa	18.9675	23.36111	31.55893	294.3714				290.7456	56.58325	69.29564	80.8613	209.6234	74.70912	106.0761	119.0039	191.68-JC
Modulus	72.68823	76.58436	87.96991						224.6232	251.1755	283.3902		165.6624	324.6975	248.9275	
Hysteresisloss	4.00693	6.41783	8.058122						5.643561	9.518839	11.50949		12.03943	20.45717	22.07843	
Energy Absorbed	2.329374	3.395394	4.384342						3.77939	5.849674	6.72493		7.726292	12.56458	12.57744	

GRADE4DEGENERATION-5029																
	Tension								Shear							
	Anterior				Posterior				Anterior				Posterior			
	Slow	Medium	Fast	Fail - Pccrashed anddidnot recordthef ullfailure	Slow	Medium	Fast	Fail	Slow	Medium	Fast	Fail	Slow	Medium	Fast	Fail
Maxforce/mN	506	650	795	3505	295	602	954	8263	794	1300	1761	3468	1259	2695	3138	7186
MaxStress/kPa	15.21713	19.5477	23.90834	270.2301	11.55051	23.57087	37.35317	270.5632	32.86968	53.81686	72.90114	80.900003	49.30231	105.5359	122.8838	21.22936
Modulus	51.64402	55.80912	58.22958		11.67001	57.54697	105.7397		107.3813	203.3403	337.4863		354.2769	519.1521	517.7467	
Hysteresisloss	4.159777	5.710622	4.507159		2.834136	7.134272	12.65884		4.17013	7.785071	10.87337		6.117142	14.73364	16.61882	
Energy Absorbed																

GRADE4 GL1911813																
	Tension								Shear							
	Anterior				Posterior-worsegraph				Anterior				Posterior			
	Slow	Medium	Fast	Fail	Slow	Medium	Fast	Fail	Slow	Medium	Fast	Fail	Slow	Medium	Fast	Fail
Maxforce/mN	189	568	821	4634	157	175	193	528	778	597	805	1564	1863	2098	2332	3073
MaxStress/kPa	14.08346	42.32489	61.17735	345.3055	14.75564	16.44	18.1391	49.62406	38.02542	29.17889	39.34506	76.44184	46.00204	51.80477	57.58281	75.87992
Modulus	46.19783	65.82185	90.53338		28.54182	24.21383	33.8513		144.0827	121.1905	241.2019		288.2351	303.1881	337.8544	
Hysteresisloss	10.98649	16.73913	31.47658		9.172328	9.151047	10.68448		5.210174	5.210381	7.127361		4.567911	5.976612	5.85662	
Energy Absorbed	1.395791	9.16016	15.99887		4.855397	4.731102	5.480162		3.202157	3.058077	3.982999		3.030863	3.554246	3.317516	

Average modulus

	Grade 2					
	Anterior-Tension			Posterior-Tension		
Specimens	Slow	medium	fast	slow	med	fast
1	42.45231	62.25284	63.3834	13.64413	43.60025	45.52399
2	111.2695	252.9564	291.7524	56.34698	73.60967	87.63527
2	82.21649	144.4022	156.1621	37.53969	40.3776	44.30301
4	53.32017	85.29284	71.7365	35.8436	52.52917333	59.15409
5		45.79706	65.75651			
AVG	72.3146175	118.14027	129.75818			
	Anterior-Shear			Posterior- Shear		
	Slow	medium	fast	Slow	medium	fast
1	893	1058.774	1141.505	162.0174	163.6489	147.6703
2	826.2718	1038.095	1099.289	242.072	280.7857	356.0212
2	423.107	358.6926	189.8322	779.7334	914.899	830.9146
4	473.2837	583.9287	576.1084	63.665	92.92931	96.31539
5	207.5705	214.5898	253.5202	112.5237	519.6713	591.6981
AVG	564.6466	650.81602	652.05096	272.0023	394.386842	404.52392
	Grade 4					
	Anterior- Tension			Posterior- Tension		
	Slow	med	fast	Slow	med	fast
1	295.2332	166.9207	286.0159	71.41625	76.78481	179.042
2	193.8486	281.4897	263.7709	77.60698	106.268	168.6368
2	72.68823	86.58436	87.96991	11.67001	57.54697	105.7397
4	51.64402	65.80912	58.22958	28.54182	24.21383	33.8513
5	46.19783	65.82185	90.53338	47.308765	66.2034025	121.81745
AVG	131.922376	133.32515	157.30393			
	Anterior-Shear			Posterior- Shear		
	Slow	med	fast	Slow	med	fast
1	144.2322	144.371	188.6386	109.9565	111.4619	113.6563
2	397.3878	490.8692	538.3521	165.6624	324.6975	248.9275
2	224.6232	251.1755	283.3902	354.2769	519.1521	517.7467
4	107.3813	203.3403	337.4863	288.2351	303.1881	337.8544
5	144.0827	121.1905	241.2019	278.2279	410.6348	543.8788
AVG	203.54144	242.1893	317.81382	239.27176	333.82688	352.41274

			MEAN		SD	
Region	Direction	Rate	Grade 2	Grade 4	Grade 2	Grade 4
		Slow	72.3146175	131.922376	40.625072	110.6632
		Medium	118.140268	133.325146	88.281644	98.08567
	Tension	Fast	129.758182	157.303934	101.7626	115.1639
		Slow	564.6466	203.54144	344.42743	132.0375
		Medium	650.81602	242.1893	434.53039	164.0263
Anterior	Shear	Fast	652.05096	317.81382	483.05758	175.675
		Slow	35.8436	47.308765	23.979911	33.99261
		Medium	52.52917333	66.2034025	28.93457	40.77563
	Tension	Fast	59.15409	121.81745	34.556587	78.37091
		Slow	272.0023	239.27176	282.49947	130.3978
		Medium	394.386842	333.82688	337.63967	190.1679
Posterior	Shear	Fast	404.523918	352.41274	320.36795	215.6386

Average hysteresis loss coefficient

	Grade 2					
	Anterior-Tension			Posterior-Tension		
Specimens	Slow	medium	fast	slow	med	fast
1	1.65	1.8	1.87	1.62	1.76	1.85
2	2.18	2.22	2.71	1.57	1.79	1.77
2	1.8	1.85	1.86	1.63	1.65	1.72
4	1.72	1.83	1.85	1.81	1.84	1.85
5		1.77	1.7			
AVG	1.8375	1.894	1.998	1.6575	1.76	1.7975
	Anterior-Shear			Posterior- Shear		
	Slow	medium	fast	Slow	medium	fast
1	1.55	1.7	8.05	1.64	1.61	1.72
2	1.7	1.7	1.74	1.59	1.69	1.75
2	1.68	1.67	1.75	1.46	1.59	1.75
4	1.52	1.64	1.73	1.68	1.62	1.75
5	1.47	1.55	1.63			
AVG	1.584	1.652	2.98	1.5925	1.6275	1.7425
	Grade 4					
	Anterior- Tension			Posterior- Tension		
	Slow	med	fast	Slow	med	fast
1	1.69	1.84	1.92	1.66	1.84	1.92
2	1.72	1.79	1.85	1.47	1.7	1.79
2	1.72	1.89	1.84	1.59	1.68	1.83
4	1.6	1.66	1.03	1.89	1.93	1.95
5	7.87	1.83	1.97			
AVG	2.92	1.802	1.722	1.6525	1.7875	1.8725
	Anterior-Shear			Posterior- Shear		
	Slow	med	fast	Slow	med	fast
1	1.76	1.8	1.86	1.51	1.64	1.74
2	1.68	1.74	1.8	1.56	1.63	1.76
2	1.49	1.63	1.71	1.58	1.68	7
4	1.36	1.59	1.7	1.51	1.68	1.77
5	1.63	1.7	1.79			
AVG	1.584	1.692	1.772	1.54	1.6575	3.0675

			MEAN		SD	
Region	Direction	Rate	Grade 2	Grade 4	Grade 2	Grade 4
		Slow	1.8375	2.92	0.988534	2.616988
		Medium	1.894	1.802	1.27874	1.307895
	Tension	Fast	1.998	1.722	1.277739	1.383061
		Slow	1.584	1.584	1.397507	1.401823
		Medium	1.652	1.692	1.367947	1.352578
Anterior	Shear	Fast	2.98	1.772	2.666111	1.319182
		Slow	1.6575	1.6525	1.051537	1.060929
		Medium	1.76	1.7875	1.004176	0.994786
	Tension	Fast	1.7975	1.8725	0.986544	0.953661
		Slow	1.5925	1.54	1.079852	1.100577
		Medium	1.6275	1.6575	1.061683	1.047845
Posterior	Shear	Fast	1.7425	3.0675	1.009668	2.308437

Average failure stress

	Grade 2	
Specimens	Anterior-Failure Stress-Tension	Posterior-Failure stress-Tension
1	238.9243	64.9976
2	340.7036	320.2044
3	206.25349	279.3771
4	222.7936	
5	469.9275	
AVG	295.720498	221.5263667
	Anterior-Failure Stress-Shear	Posterior-Failure Stress-Shear
1	211.0549	23.50393
2	224.9357	96.97203
3	73.61292	197.2877
4	129.201	32.71402
5	89.18507	84.2884
AVG	145.597918	86.953216
	Grade 4	
	Anterior-Failure Stress-Tension	Posterior-Failure stress-Tension
1	166.9788	110.05
2	294.3714	290.7456
3	270.2301	270.5632
4	345.3055	49.62406
5		
AVG	269.22145	180.245715
	Anterior-Failure Stress-Shear	Posterior-Failure Stress-Shear
1	55.92784	44.01671
2	209.6234	191.68
3	80.90003	21.22936
4	76.44184	75.87992
5		
AVG	105.7232775	83.2014975

			MEAN		SD	
Region	Direction		Grade 2	Grade 4	Grade 2	Grade 4
Anterior	Tension		295.7205	269.2215	154.5005	135.2311
	Shear		221.5264	105.7233	84.48119	75.87245
Posterior	Tension		221.5264	180.2457	156.4189	129.6215
	Shear		86.95322	83.2015	70.4923	74.5243

Average energy absorption at failure

Failure G2		
	Anterior_Tension	Anterior_Shear
4696	342.7334	58.53738
123	857.6463	205.309
406	806.8867	147.8488
864	269.9795	87.17133
781		65.91451
AVG	569.311475	112.956204
	P_T	P_S
4696	81.7916	137.5698
123	308.5164	23.12562
781	1477.518	68.12711
864	178.9185	73.51797
406		15.9189
AVG	511.686125	63.65188
Failure G4		
	Anterior_Tension	Anterior_Shear
4889	623.8938	256.588
5029	657.69	54.13
5194	1803.438	67.69
471	451.9721	15.0467
	884.248475	98.363675
	P_T	P_S
4889	1085.33	307.0740133
5029	2129.29	11.4347
5194	157.9346	23.3551
471	163.198	38.158255
AVG	883.93815	95.00551708

		MEAN		SD	
Region	Direction	Grade 2	Grade 4	Grade 2	Grade 4
Anterior	Tension	569.3115	884.2485	366.1208	665.3487
	Shear	112.9562	98.36368	71.13064	102.4668
Posterior	Tension	511.6861	883.9382	607.4226	902.419
	Shear	511.6861	95.00552	49.7368	129.3717

Appendix D

Modulus

Tests of Within-Subjects Effects

Measure: MEASURE_1

Source		Type III Sum of Squares	df	Mean Square	F	Sig.
modulus	Sphericity Assumed	114833.841	2	57416.921	12.854	<.001
	Greenhouse-Geisser	114833.841	1.341	85650.643	12.854	<.001
	Huynh-Feldt	114833.841	1.721	66717.836	12.854	<.001
	Lower-bound	114833.841	1.000	114833.841	12.854	.001
modulus * Grade	Sphericity Assumed	6881.421	2	3440.710	.770	.468
	Greenhouse-Geisser	6881.421	1.341	5132.617	.770	.422
	Huynh-Feldt	6881.421	1.721	3998.068	.770	.450
	Lower-bound	6881.421	1.000	6881.421	.770	.387
modulus * Region	Sphericity Assumed	1500.718	2	750.359	.168	.846
	Greenhouse-Geisser	1500.718	1.341	1119.334	.168	.757
	Huynh-Feldt	1500.718	1.721	871.909	.168	.814
	Lower-bound	1500.718	1.000	1500.718	.168	.685
modulus * Loading_Direction	Sphericity Assumed	20458.925	2	10229.463	2.290	.110
	Greenhouse-Geisser	20458.925	1.341	15259.614	2.290	.131
	Huynh-Feldt	20458.925	1.721	11886.524	2.290	.119
	Lower-bound	20458.925	1.000	20458.925	2.290	.141
modulus * Grade * Region	Sphericity Assumed	2428.059	2	1214.029	.272	.763
	Greenhouse-Geisser	2428.059	1.341	1811.006	.272	.673
	Huynh-Feldt	2428.059	1.721	1410.689	.272	.730
	Lower-bound	2428.059	1.000	2428.059	.272	.606
modulus * Grade * Loading_Direction	Sphericity Assumed	105.686	2	52.843	.012	.988
	Greenhouse-Geisser	105.686	1.341	78.828	.012	.957
	Huynh-Feldt	105.686	1.721	61.403	.012	.980
	Lower-bound	105.686	1.000	105.686	.012	.914
modulus * Region * Loading_Direction	Sphericity Assumed	4399.011	2	2199.506	.492	.614
	Greenhouse-Geisser	4399.011	1.341	3281.073	.492	.541
	Huynh-Feldt	4399.011	1.721	2555.802	.492	.586
	Lower-bound	4399.011	1.000	4399.011	.492	.488
modulus * Grade * Region * Loading_Direction	Sphericity Assumed	4743.244	2	2371.622	.531	.591
	Greenhouse-Geisser	4743.244	1.341	3537.824	.531	.522
	Huynh-Feldt	4743.244	1.721	2755.799	.531	.565
	Lower-bound	4743.244	1.000	4743.244	.531	.472
Error(modulus)	Sphericity Assumed	259075.068	58	4466.812		
	Greenhouse-Geisser	259075.068	38.881	6663.285		
	Huynh-Feldt	259075.068	49.914	5190.386		
	Lower-bound	259075.068	29.000	8933.623		

Hysteresis loss coefficient

Tests of Within-Subjects Effects

Measure: MEASURE_1

Source		Type III Sum of Squares	df	Mean Square	F	Sig.
hlc	Sphericity Assumed	.952	2	.476	.647	.527
	Greenhouse-Geisser	.952	1.624	.586	.647	.497
	Huynh-Feldt	.952	2.000	.476	.647	.527
	Lower-bound	.952	1.000	.952	.647	.428
hlc * Grade	Sphericity Assumed	1.704	2	.852	1.159	.321
	Greenhouse-Geisser	1.704	1.624	1.049	1.159	.314
	Huynh-Feldt	1.704	2.000	.852	1.159	.321
	Lower-bound	1.704	1.000	1.704	1.159	.291
hlc * Region	Sphericity Assumed	.537	2	.268	.365	.696
	Greenhouse-Geisser	.537	1.624	.331	.365	.652
	Huynh-Feldt	.537	2.000	.268	.365	.696
	Lower-bound	.537	1.000	.537	.365	.551
hlc * Loading_Direction	Sphericity Assumed	1.739	2	.870	1.183	.314
	Greenhouse-Geisser	1.739	1.624	1.071	1.183	.308
	Huynh-Feldt	1.739	2.000	.870	1.183	.314
	Lower-bound	1.739	1.000	1.739	1.183	.286
hlc * Grade * Region	Sphericity Assumed	2.125	2	1.062	1.445	.244
	Greenhouse-Geisser	2.125	1.624	1.308	1.445	.246
	Huynh-Feldt	2.125	2.000	1.062	1.445	.244
	Lower-bound	2.125	1.000	2.125	1.445	.239
hlc * Grade * Loading_Direction	Sphericity Assumed	.533	2	.266	.362	.698
	Greenhouse-Geisser	.533	1.624	.328	.362	.654
	Huynh-Feldt	.533	2.000	.266	.362	.698
	Lower-bound	.533	1.000	.533	.362	.552
hlc * Region * Loading_Direction	Sphericity Assumed	1.759	2	.879	1.196	.310
	Greenhouse-Geisser	1.759	1.624	1.083	1.196	.304
	Huynh-Feldt	1.759	2.000	.879	1.196	.310
	Lower-bound	1.759	1.000	1.759	1.196	.283
hlc * Grade * Region * Loading_Direction	Sphericity Assumed	.412	2	.206	.280	.757
	Greenhouse-Geisser	.412	1.624	.254	.280	.711
	Huynh-Feldt	.412	2.000	.206	.280	.757
	Lower-bound	.412	1.000	.412	.280	.601
Error(hlc)	Sphericity Assumed	41.176	56	.735		
	Greenhouse-Geisser	41.176	45.467	.906		
	Huynh-Feldt	41.176	56.000	.735		
	Lower-bound	41.176	28.000	1.471		

Failure stress

Tests of Between-Subjects Effects

Dependent Variable: Failure_stress

Source	Type III Sum of Squares	df	Mean Square	F	Sig.
Corrected Model	172484.822[a]	7	24640.689	3.306	.010
Intercept	1033913.173	1	1033913.173	138.705	<.001
Grade	2566.732	1	2566.732	.344	.562
Region	5821.337	1	5821.337	.781	.384
Loading_Direction	137643.203	1	137643.203	18.466	<.001
Grade * Region	585.984	1	585.984	.079	.781
Grade * Loading_Direction	7980.037	1	7980.037	1.071	.309
Region * Loading_Direction	891.529	1	891.529	.120	.732
Grade * Region * Loading_Direction	5250.675	1	5250.675	.704	.408
Error	223621.628	30	7454.054		
Total	1388597.676	38			
Corrected Total	396106.450	37			

a. R Squared = .435 (Adjusted R Squared = .304)

Energy absorption at failure

Tests of Between-Subjects Effects

Dependent Variable: Failure_EA

Source	Type III Sum of Squares	df	Mean Square	F	Sig.
Corrected Model	3761430.685[a]	7	537347.241	2.566	.038
Intercept	5469658.407	1	5469658.407	26.119	<.001
Grade	257450.576	1	257450.576	1.229	.278
Region	7521.828	1	7521.828	.036	.851
Loading_Direction	3258376.345	1	3258376.345	15.560	<.001
Grade * Region	6626.538	1	6626.538	.032	.860
Grade * Loading_Direction	230289.005	1	230289.005	1.100	.304
Region * Loading_Direction	50.805	1	50.805	.000	.988
Grade * Region * Loading_Direction	133.410	1	133.410	.001	.980
Error	5444734.569	26	209412.868		
Total	14229871.789	34			
Corrected Total	9206165.254	33			

a. R Squared = .409 (Adjusted R Squared = .249)